

Lawrence Berkeley National Laboratory

Recent Work

Title

A FEASIBILITY STUDY OF THE THERAPEUTIC POSSIBILITIES

Permalink

<https://escholarship.org/uc/item/6r63w99k>

Author

Aceto, Henry

Publication Date

1964-06-01

UCRL-11482

University of California

Ernest O. Lawrence
Radiation Laboratory

A FEASIBILITY STUDY OF
THE THERAPEUTIC POSSIBILITIES OF π^- MESONS

TWO-WEEK LOAN COPY

*This is a Library Circulating Copy
which may be borrowed for two weeks.
For a personal retention copy, call
Tech. Info. Division, Ext. 5545*

DISCLAIMER

This document was prepared as an account of work sponsored by the United States Government. While this document is believed to contain correct information, neither the United States Government nor any agency thereof, nor the Regents of the University of California, nor any of their employees, makes any warranty, express or implied, or assumes any legal responsibility for the accuracy, completeness, or usefulness of any information, apparatus, product, or process disclosed, or represents that its use would not infringe privately owned rights. Reference herein to any specific commercial product, process, or service by its trade name, trademark, manufacturer, or otherwise, does not necessarily constitute or imply its endorsement, recommendation, or favoring by the United States Government or any agency thereof, or the Regents of the University of California. The views and opinions of authors expressed herein do not necessarily state or reflect those of the United States Government or any agency thereof or the Regents of the University of California.

Research and Development

UCRL-11482

UNIVERSITY OF CALIFORNIA
Lawrence Radiation Laboratory
Berkeley, California
AEC Contract No. W-7405-eng-48

A FEASIBILITY STUDY OF THE THERAPEUTIC POSSIBILITIES
OF π^- MESONS

Henry Aceto, Jr.
(Ph. D. Thesis)

June 10, 1964

A FEASIBILITY STUDY OF THE THERAPEUTIC POSSIBILITIES
OF π^- MESONS

Henry Aceto, Jr.

Lawrence Radiation Laboratory
University of California
Berkeley, California

ABSTRACT

The feasibility of extending the arsenal of heavy particles available in radiotherapy to include pi negative mesons is investigated by employing several dosimetric techniques. From the data obtained a preliminary assessment of the possibilities of pi negative mesons is discussed. The results are indicative of many possible advantages, both in improving radiotherapeutic techniques and in offering new areas for basic radiobiologic investigations.

A FEASIBILITY STUDY OF THE THERAPEUTIC POSSIBILITIES
OF π^- MESONS

Contents

Abstract	
I. Introduction	1
II. Experimental Method	
A. Pion Beam	
1. Beam Dynamics	11
2. Beam Analysis	18
B. Detection Techniques	
1. Ionization Chambers	25
2. Scintillation Detectors	28
a. Integral Range Apparatus	31
b. Beam Profile Apparatus	31
3. Semiconductor Detectors	35
4. Thermoluminescence	41
5. Photographic Film	46
C. Counting Losses	48
III. Theory	
A. Interaction of Charged Particles With Matter	
1. Energy Loss Formula	52
2. Linear Energy Transfer	63
3. Bragg Curve	64
B. Meson Production	66
C. Meson Decay and Interactions	72
IV. Results and Discussion	79
V. Concluding Remarks	107
Acknowledgments	111
Bibliography	112
Vita	118

I. INTRODUCTION

It is well known that injury to normal tissue is one of the major obstacles to improved effectiveness of radiation therapy of tumors. Injury to tissues brings about in patients both early adverse reactions to radiation and more remote complications. The complications that result are often so serious that one must not only lower the tumor dose, but even entirely discontinue the radiation therapy. Thus it is essential to find means of selectively lowering the integral dose delivered to healthy tissue relative to that in the tumor and thereby increasing correspondingly the therapeutic action on deep-seated malignant neoplasms.

In recent years the application of high-energy machines to therapeutic radiology and associated radiobiologic investigations has been an important step in attacking this problem. Thus by means of a cyclotron, a betatron, a synchrotron, or a linear accelerator one may obtain a well-collimated beam of high-energy protons, electrons, photons, neutrons, α particles, mesons, or heavy ions up to argon. Each of these radiations is characterized by properties that enhance its usefulness for certain applications while limiting it in others.

High-energy x-ray beams have been shown to exhibit a depth-dose curve, with a relatively low skin dose, that rises to a maximum and then decays exponentially on the exit side.¹ In tissue, the beam spreads beyond its original angular divergence, owing to multiple scattering and production of secondaries. The depth of maximum ionization increases almost linearly with energy; the resultant peaks are quite broad, and the intensity drops off very slowly thereafter. At energies higher than about 20 MeV the exit dose is almost as large as that received at the maximum position. Even when the dosage to the healthy tissue is distributed by employing several differently oriented fields, the resulting toxemia is commonly the factor limiting

the amount of radiation that can be delivered to the tumor.

In electron therapy, ideally, the electron beam has a single well-established range,² and its degree of penetration into tissues may be regulated at will by regulating its mean energy. Since the ionization density for electrons is fairly constant above 1 MeV, we would expect nearly constant dosage, with a slight rise near the end of the range and zero dosage beyond.³ However, in actuality, a high degree of multiple scattering combined with energy loss through bremsstrahlung processes increases the total inherent straggling to as much as 30% of the mean range.⁴ Consequently, there is a considerable decrease of the LET (linear energy transfer) with increased depth, and virtual obliteration of the hypothetical ionization peak at the end of the range.

To summarize the improvements in radiation therapy made possible by use of high-energy x rays and electrons for direct tumor therapy, one may generally say that these radiations are suitable when we wish to irradiate surface layers or to give uniform dose over a relatively large region deep in tissue.

On the other hand, highly localized lesions in accurately predetermined positions in the body should be most effectively produced by heavy charged particles (charged particles heavier than electrons). These particles have unique characteristics that make them extremely attractive both for improving radiotherapeutic techniques and for offering new fields of basic radiobiologic investigation. They show a definite range with deep penetration and far less scattering than electrons, accompanied by a most favorable distribution of energy loss. The initial portion of the energy-loss pattern is represented by a relatively broad flat plateau region (or minimum-ionizing region), which is followed by a rapid rise in ionization caused by the increasing rate of energy loss with decreasing particle velocity. As the particle velocity continues to decrease, the gradual charge neutralization

begins to dominate the velocity dependence, and the ionization comes to a maximum at the "Bragg peak" just before the end of the range of the particles. The complete ionization distribution, including both the minimum-ionizing region and the Bragg peak region of maximum ionization, constitutes what is commonly known as the Bragg curve. The peak-to-plateau ionization ratio of the curve can be readily converted to a tissue-dose ratio. This ratio may represent an extreme advantage in depth dose, whereby high doses can be delivered at almost any desired predetermined depth in tissue, with intervening and deeper layers of tissue receiving very much lower doses. These unique qualities make this radiation physically well suited for relatively precise irradiation of both deep-seated tumors and superficial tumors adjacent to radiosensitive tissue.

Beginning in 1952, the possibility of applying these heavy atomic particles to therapy stimulated radiological experiments by several investigators.^{5,6,7} Until that time, the only heavy nucleons used in therapeutic clinical studies were neutrons. Of course, the neutron does not exhibit a Bragg curve, but displays an attenuation curve quite similar to that of electrons. Nevertheless, the early work of Lawrence et al. suggested that neutrons, by virtue of their relatively high-LET secondary protons, produce a greater biological effect on normal and neoplastic tissues than do x rays.⁸

Subsequent neutron radiotherapy, however, has yielded results that showed no favorable selective effects.⁹ More recently, Fowler et al. have revived interest with a series of pretherapeutic experiments with a neutron beam, designed to elucidate the problems inherent in neutron therapy and specifically to explain the long-term injury to normal tissues reported by Stone.¹⁰ Moreover, an important ever-present consideration in neutron therapy is that there is always a compromise between higher LET's obtained with lower-energy neutrons on the one hand, and better depth doses with higher-energy

neutrons on the other. Furthermore, investigations, with neutrons, of LET effect upon radiobiological action has serious limitations: even with monoenergetic neutrons, the LET spectrum is quite broad, owing to the dominant elastic collision cross section, which results in a secondary-proton spectrum ranging from the incident neutron energy down to nearly zero energy. Consequently, radiobiological research studies on the cellular level, for instance, may become quite difficult to analyze, since a given cell may be irradiated by a secondary particle with any energy (and therefore almost any LET) extending over the total range.

Investigations using protons, deuterons, and alpha particles were designed primarily to gain fundamental knowledge concerning their biological effectiveness and mechanism of lethal action. These studies revealed that by using rotation techniques or taking advantage of the Bragg curve a sizable amount of energy can be preferentially delivered to localized areas of the body. For example, a beam of high-energy protons, suitably attenuated, was passed through the body of a mouse; the degradation was just sufficient to place the Bragg peak at the site of a transplantable tumor on the opposite side of the animal, and the neoplasm was destroyed. These encouraging results have led to the use of the Bragg peak to treat soft-tissue and brain tumors directly.^{11,12} At the Bragg peak not only is the actual dose greater than the skin dose, but the increased ionization at the peak, with its concomitant increase in LET, produces a greater RBE as well. This is to be expected, since numerous radiobiological investigations have shown that the total dose required to produce a given biological effect is not constant, but may vary considerably with LET. It has been established that in order to evaluate the effects of irradiation, one must know both the total energy deposited within a given volume (or rad dose) and the spatial distribution of the energy within that volume (or the LET).¹³ The work of Berendsen et al., using human kidney

cells in tissue culture, is in general agreement with other studies in that the RBE is shown to increase with LET up to about 100 keV/ μ , after which it decreases for still higher LET values.^{14,15} This additional advantage of a greater RBE for each unit of absorbed dose at the peak than at the plateau has been confirmed by in vivo experiments with two different ascites tumors (a lymphoma and a mammary carcinoma).¹⁶ Also, Larsson reported an RBE of 0.7 for minimum-ionizing 170-MeV protons for producing chromosome aberrations in Allium and Vicia,¹⁷ with a significant increase in RBE toward the end of the Bragg peak.

However, it is important to note at this point that protons give rise to serious problems in this connection, in that the Bragg peak is too narrow to permit uniform irradiation of tumors generally found in man. Furthermore, fast proton beams do not have very high LET's except in the small terminal portion of their travel. By introduction of various thicknesses of absorber the Bragg peak may be transformed into flat maxima of various lengths, corresponding to the tumor dimensions, by overlapping of different proton energies.¹⁸ However, this transformation and its associated redistribution of the proton energy over a larger volume is achieved at the cost of the peak-to-plateau depth-dose advantage, and markedly decreases the average LET in the Bragg peak region. On the other hand, the highly localized narrow Bragg peak does have extreme advantage for certain neurologic applications requiring production of very small well-defined lesions. In particular, one of the early methods of treatment of patients with acromegaly, advanced breast cancer, or malignant diabetes with retinopathy involved the difficult procedure of surgical hypophysectomy. It soon became apparent that high-energy particles should be effective in radiosurgery, such as in inhibiting pituitary function or for pituitary ablation, thereby sparing the patient the trauma and associated complications of surgical hypophysectomy. Tobias et al. have successfully

applied this radiosurgical technique to produce destructive lesions in the pituitary of rats, dogs, and monkeys with beams of high-energy deuterons or protons.^{5,19} Despite this success and the obvious theoretical advantages, there are many difficulties involved in using the Bragg curve in treating patients. Particularly in pituitary irradiation, it is absolutely necessary to avoid irradiating the vital structures surrounding the hypophysis, such as the optic tracts, hypothalamus, and the various cranial nerves. Although the pituitary can be fairly accurately located by taking x-ray photographs, the Bragg peak cannot be positioned with equal accuracy, owing to the heterogeneity of the irradiated body mass, and therefore one is forced to use continuous head rotation (with the beam incident on the pituitary at the center of rotation) to obtain the increased dose to the pituitary. However, in this case there is no added increment contributed by a Bragg peak and its associated increased RBE. On the other hand, if one were able to accurately assess the degree of inhomogeneity in the region surrounding the point of irradiation, then proper adjustment could be made for the departure from a homogeneous medium, and the peak position could be determined with reasonable accuracy.

The Bragg peak has added significance through its relation to still another possible advantage of heavy particles in therapy. This radiotherapeutic advantage lies in their relation to the oxygen effect.

It has been known for a long time either both normal or malignant tissue that is poorly supplied with oxygen at the time of irradiation experiences less biological damage by a given dose of x and γ rays than the same tissue when well supplied with oxygen. More than 50 years ago Schwarz observed that human skin reaction to radiation was diminished when blood flow was restricted, either by compression or suction.²⁰ Still today, the complex nature of the oxygen effect cannot be regarded as completely elucidated. On the one hand, oxygen exerts its action by virtue of an indirect effect due to radiation, through its role as an active participant in the formation of active radicals and

peroxides. On the other hand, it is also involved in the direct action of radiation (i. e., when free radicals formed in H_2O are not involved).²¹

The relevance of the oxygen effect to radiotherapy depends upon a supposed differential between the radiosensitivity of normal tissue and a tumor, owing in part to the impaired circulation to necrotic regions of the tumor and concomitant anoxia (in relation to those regions where oxygen supply has not been affected). That is, the anoxic cells are not killed as readily by x rays and γ rays as are well-oxygenated healthy cells. The maximum oxygen effect is reached at an oxygen content in the medium surrounding the object being irradiated that corresponds to the concentration of oxygen in the air (approximately 21%). A further increase of the oxygen tension has no effect on the radiation sensitivity of the object. This behavior is of great importance in the radiation therapy of tumors because of the considerably lower oxygen concentration in malignant neoplasms than in normal tissue. It follows from this that increasing the supply of oxygen at the moment of irradiation will lead to a considerable increase in the radiosensitivity of tumors, while that in normal, well-oxygenated tissue remains practically unchanged, since they are already at maximum radiosensitivity. This approach is the basis of the studies by Churchill-Davidson, in which the patient is subjected to oxygen tensions as high as 2 or 3 atmospheres.²²

An equally promising and somewhat less severe approach to this problem of effectively overcoming the anoxic cells is to use radiation of a quality which causes cell injury irrespective of the oxygen differential (i. e., high-LET radiation). Many experiments such as those on unicellular organisms by Howard-Flanders²³ and Berendson,²⁴ using a tissue culture, have confirmed that the presence or absence of oxygen has less influence on the radiobiological responses to high-LET radiations than to low-LET radiations. Gray has reported the radiosensitivity of Ehrlich ascites tumor cells irradiated by fast neutrons to

be much less affected by oxygen concentration than when irradiated with x rays.²⁵ Lawrence, using heavier charged particle beams, has indicated similar findings.⁴⁶

The oxygen-enhancement factor varies with the type of radiation used, being highest with radiations of lowest LET. With x rays the biological effect produced is approximately three times as great under aerobic conditions as under anaerobic conditions (i. e., oxygen enhancement factor ≈ 3). In contrast, this same ratio for the killing of mouse ascites tumor cells, as reported by Hornsey and Silini, is 1.9 for neutrons of mean energy (6 MeV), whose average LET is approximately 20 keV/ μ .²⁶ Although this ratio is much lower than the corresponding x-ray values, there is still an appreciable and undesirable oxygen differential effect. The ratio of the oxygen-enhancement factor for x rays to that for neutrons, m_x/m_n , gives the "gain factor" in treating anoxic cells. For equal injury to well-oxygenated tissues, the effect on anoxic cells is increased as if the dose to only these cells had been increased by an amount equal to the gain factor. This gain factor is identical with the ratio of the RBE's for anoxic and oxygenated cells.

This is of great importance, particularly because the dose of radiation applied in therapy must be large enough to destroy all tumor cells. If even single uninjured cells remain after radiation therapy, this is enough for regeneration of the tumor.²⁷ Human tumors consist of an agglomeration of cells which vary widely with respect to the oxygen tension in them. Among them there may always be present a small number of cells which for all practical purposes are under anaerobic conditions (and therefore are highly resistant to radiation), but have not lost their capacity to proliferate. In cases like this it is of particular importance to increase the radiation sensitivity of the tumor cells to the maximum possible extent, because the success of the radiation therapy depends on whether or not the few resistant cells are killed.

The purpose of this study is to extend the arsenal of heavy particles available to include the π^- meson. The therapeutic possibilities of π^- meson beams was recognized very early by Richman, and was later discussed by Wilson⁴ and Tobias.²⁸ Likewise, Fowler and Perkins have concretely demonstrated the potential usefulness of π^- mesons with some theoretical depth-dose calculations.²⁹ Nevertheless, virtually no experimental investigation of π^- mesons has been reported thus far. The π^- meson behaves like any other heavy charged particle in its traversal through matter in that it exhibits the familiar Bragg curve and has a definite range. However, unlike the other charged particles, the π^- meson, as it is brought to rest at the end of its range in tissue, is captured by the heavier elements--mainly carbon, oxygen, and nitrogen--and it cascades down the energy levels of the atom in a time short compared with its lifetime. From the lowest atomic state it is captured by the nucleus, and causes it to release approximately 30 MeV per absorbed pion by exploding into a variable multiplicity of α particles and protons which are capable of delivering a large localized radiation dose. A further 70 MeV is carried off, mainly as fast neutrons, most of which escape from the tissue without an appreciable dose contribution. At any rate, we then have a Bragg curve whose peak-to-plateau ratio is augmented through this unique capture phenomenon involving the heavy charged nuclear fragments. The actual dose differential is not only greater, but also the increased ionization density of the Bragg peak, due to the high-LET nuclear fragments, contributes an added increment through its increased RBE. For pions, the degree of straggling is determined to a great extent by the initial momentum spread of the incident pion beam, which in turn controls the width of the Bragg peak. That is, instead of using attenuating material to introduce a larger spread in energies in order to obtain a wider Bragg peak (as is the case with protons) one simply manipulates the momentum acceptance of the magnetic system to obtain the desired peak width. Furthermore, the

highly ionizing α particles, of mean energy 6 MeV, resulting from the nuclear absorption event in tissue nuclei should be effective in further decreasing the differential oxygen effect below that which is presently available with existing particle beams. Indeed, herein lies what may be the most significant contribution of π^- mesons to radiotherapy.

Experimental measurements were made to quantitatively assess these theoretical possibilities.

Bragg curves were obtained for beams of different momentum spread and incident pion energies. These data provided some useful information relating the dose available from the pion beam to its distribution pattern for different operating conditions.

In addition, a determination of the probable LET of pions at various points on the Bragg curve, particularly at the Bragg peak, was also made.

From the results, one should be able to make a preliminary assessment of negative pions and their possible role in radiotherapy.

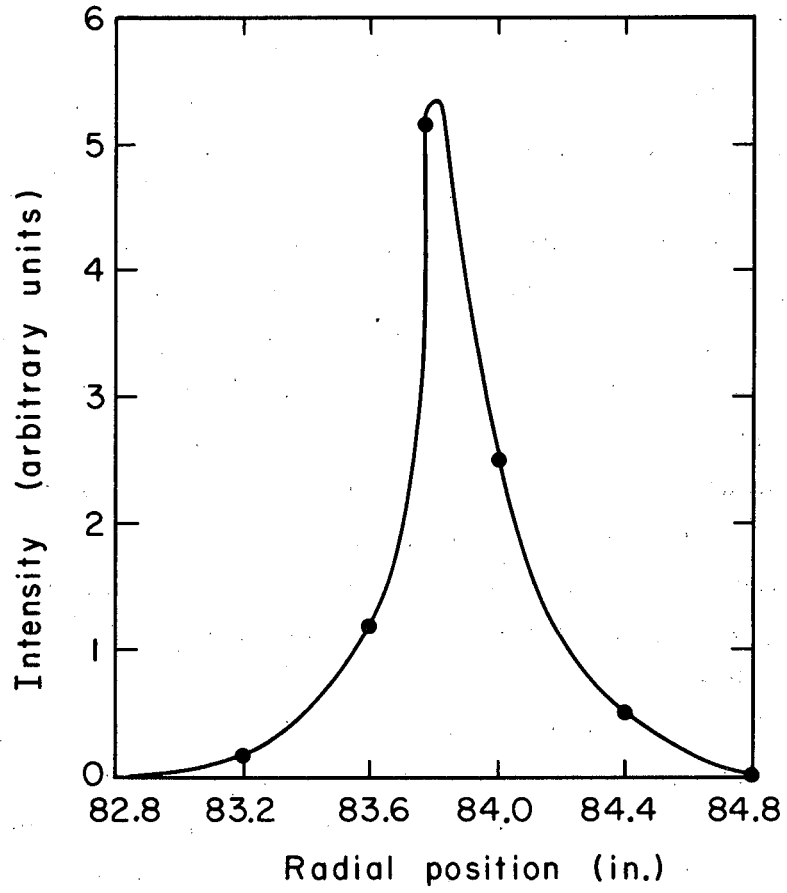
II. EXPERIMENTAL METHOD

A. Pion Beam

1. Beam Dynamics

The 732-MeV proton beam of the Berkeley 184-inch synchrocyclotron bombarded an internal beryllium target which has a cross section 1/2 inch in the radial direction by 2 inches vertically, and was 2 inches thick in the beam direction. The approximate target position in the cyclotron was taken from Astbury et al., and fine adjustments were then determined experimentally to give the maximum π^- intensity at the position of the beam monitor.³⁰ This intensity was found experimentally to be a strong function of the radial position of the target (Fig. 1). The azimuth position of the internal cyclotron target and the direction of emergence of the beam into the experimental area were determined from the known cyclotron field measurements by requiring the selected particle momentum to start tangent to the orbit corresponding to the target position and pass through the center of the meson wheel.

Mesons are produced in roughly 1% of the nuclear collisions, perhaps one meson for each 10^4 protons. The focusing conditions are best for negative mesons emitted in the roughly forward direction with respect to the proton beam, and for positive mesons emitted in the backward direction. Because of the considerable velocity of the center of mass of the collision, the average energy of the backward mesons is smaller, approximately one-half that of the forward mesons. Consequently, the highest energy of positive beams with useful intensity is less than that in the negative beams. A lower limit on the energies of both positive and negative beams is set by the inability of soft mesons to escape the fringing field. Negative and positive pions were partially momentum-analyzed by being reflected outward by the fringe field of the cyclotron and being passed through a thin aluminum window into the



MU-34173

Fig. 1. Optimization of internal Be target radial position.

magnet system. When we change from a negative to a positive pion beam, all the magnetic fields are reversed, including that of the cyclotron. A representative magnet system is shown in Fig. 2.

A two-section quadrupole magnet with an aperture of 8 inches focused the emerging beam of pions, which then passed through the meson wheel--a rotatable iron collimator 8 feet long. From the wheel the resultant parallel beam of pions entered the experimental area, or meson cave, where the final momentum analysis was performed by a bending magnet.

Further fine focusing of the pion beam was obtained by a second doublet quadrupole magnet positioned beyond the bending magnet.

Mainly for reasons of efficient cyclotron operation, the choice of bending magnet and doublet quadrupole used was dictated by the experiment in progress in the cave at the time of our run. Therefore, the magnets used in the different runs were not always the same. A complete analogy to geometric optics can be drawn in designing a magnet system for a high-energy particle beam of a particular magnetic rigidity, or momentum. The simplest system of forming this beam of secondary particles involves the use of magnetic fields only.

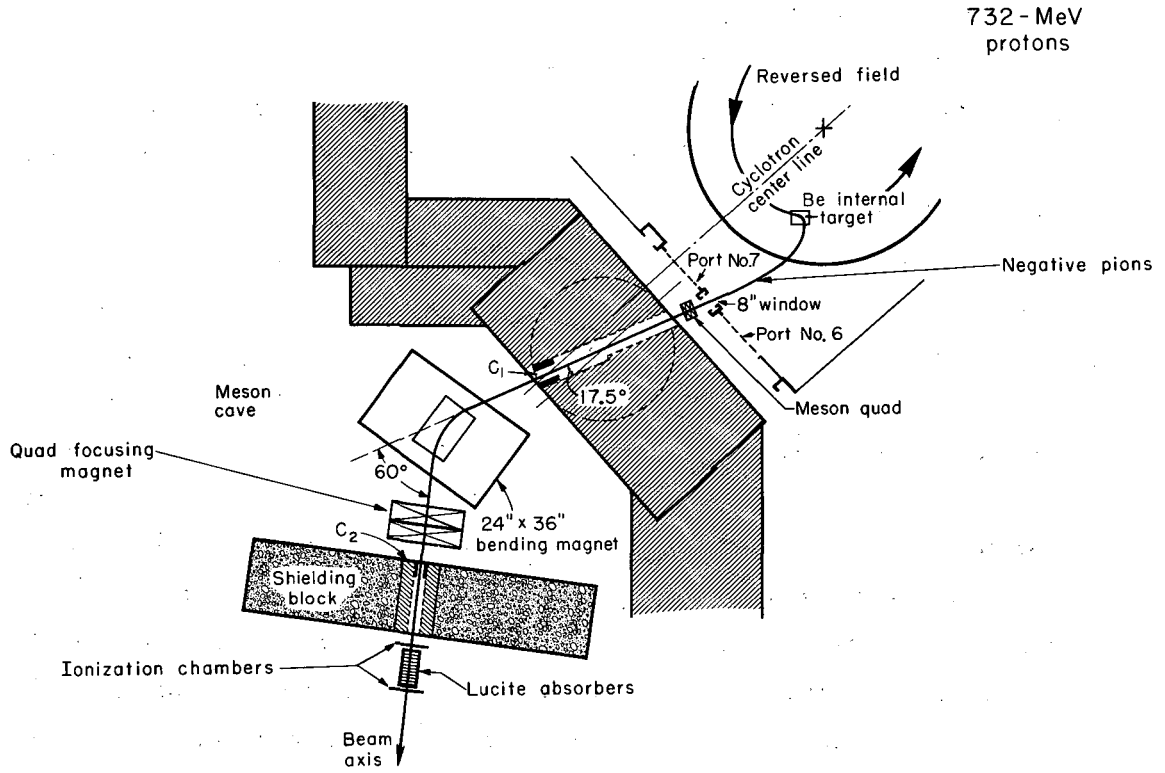
The curvature K of the path of a charged particle moving in a direction perpendicular to the direction of a magnetic field is given by

$$K = eH/pc, \quad (1)$$

where e is the charge in electrostatic units, H is the magnetic field in gauss, p is the momentum in cgs units, and c is the velocity of light in cm/sec. The curvature K is given in cm^{-1} , and is the reciprocal of the radius of curvature.

In most cases the momentum of beam particles is given in the unit MeV/c (momentum in MeV/c is numerically equal to pc in MeV).

The curvature in a magnetic field for particles of single charge and momentum, measured in MeV/c, is



MUB-966

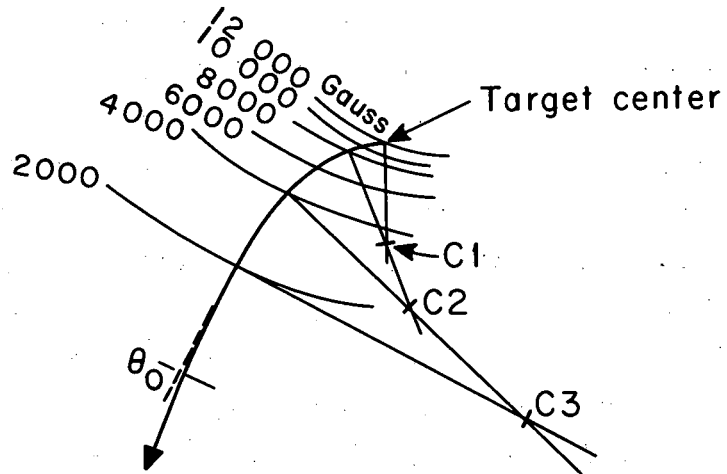
Fig. 2. The production of a negative pion beam. For the production of a positive pion beam all the magnetic fields are reversed and the proton beam is reversed. The positive pions are then taken off backward to the proton beam.

$$K = 3.00 \times 10^{-4} \quad H/p, \quad (2a)$$

$$H \rho = p(\text{MeV}/c)/3.00 \times 10^{-4}, \quad (2b)$$

where ρ is the radius of curvature in the magnetic field, H .

The magnetic field pattern has a plane of symmetry in the horizontal plane which is called the "central plane." The first magnetic component to consider is the symmetrical field of the accelerator itself, which is available in the form of contours of equal magnetic field in the central plane. From these data we may determine the central ray or central orbit out of the cyclotron for particles of a given momentum. One usually starts from a specified point, which may be the location of a target, and computes an orbit for a particle that leaves the target in some specified direction. Alternatively, one may trace the orbit in reverse, computing back from a known point toward which the particle are aimed; for example, one may compute backward from an existing collimator to determine where a target should be placed. The orbit may be graphically traced if it is approximated piecewise by circular arcs³¹ (see Fig. 3). In the figure the first arc extends from the target center on the contour of 12 kilogauss to the contour of 8 kG, being drawn with a radius of curvature appropriate to 10 kG as given by Eq. 2b. Through the end point of the first arc and through the center C1 of the first arc, the radius line can be extended to the new center C2, whose position is such as to give a new radius appropriate to the average field over the next circular arc, which is 6 kG. The second arc can then be drawn about C2 as center and extending to the 4-kG contour. This procedure is repeated out to the weak-field region, where a final deflection is used to account for the total field in that region. Of course, in practice such coarse steps should not be used, for each arc should cover only about a 20% range of field value if the final orbit is to correspond to the proper momentum to within about 1%. A 709 program has been written which performs this operation.³² The trajectory in a steering magnet may be treated in the same way. The H magnets used in this experiment are



MU-34174

Fig. 3. Graphical tracing of the orbit of a charged particle in the central plane (from Chamberlain reference 31).

designed to approximate a full uniform field within the rectangular region, and therefore the trajectory within the deflection magnet may be constructed as one circular arc.

Effective focusing of the analyzed beam is accomplished through the use of the doublet quadrupoles. Since a single quadrupole has a focusing action for motion in one plane (either horizontal or vertical) and a defocusing action in the other, a combination of two such magnets (as in the double quadrupole) serves to give a net focusing action in both planes.

The optical solutions for the external quadrupole and the angle of bend in the steering magnet used in the experiments were obtained by using OPTIK, an IBM 709 computer program which may be coupled to the program defining the beam inside the cyclotron.³³ The program represents a "beam ray" in a six-dimensional vector space, where the action of each element (bending magnet, etc.) on the vector is given by a matrix. The matrix representing the action of the field of the cyclotron was determined by solving for the horizontal and vertical focusing properties, using the cyclotron field measurements. This matrix was then used as the first element in the magnet system. The current required in the steering magnet to produce this bend was determined experimentally by the wire-orbit method.³¹ This method is based on the fact that a current-carrying wire that is under tension will take up a position coincident with the orbit of a charged particle in a magnetic field, provided the current and tension of the wire are adjusted to correspond to the momentum of the particle. The current I in the wire and tension T must satisfy the condition

$$\frac{I \text{ (in A)}}{T \text{ (in g)}} = \frac{2.94}{p \text{ (in MeV/c)}}, \quad (3)$$

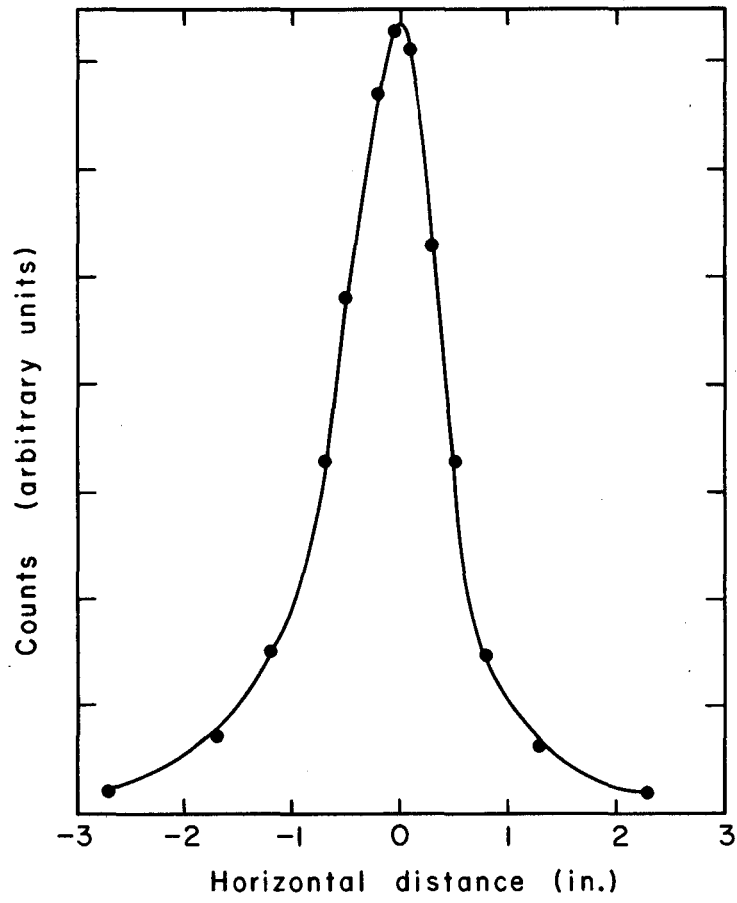
and the current must flow in the direction opposite to the beam current represented by the charged particles moving along the orbit.

2. Beam Analysis

A particularly important parameter in any dosimetric analysis of a beam is the flux-density distribution in a plane perpendicular to the direction of the beam. Such an appraisal was made from horizontal and vertical profiles of the pion beam obtained by the beam-profile counter of Solomon and Andreae.³⁴ Figures 4 and 5 indicate a typical profile taken in the horizontal and vertical directions, respectively. Measurements were made as a function of absorber thickness placed in the beam, thus yielding useful experimental information relating the degree of divergence and associated structural changes of the pion beam to depth in a phantom. These data are of particular importance in determining the effective volume for calculations of ionization chamber dose and in making a preliminary assessment of the importance of multiple Coulomb scattering events. The beam profile results, and their applications discussed here are presented in Chapter IV.

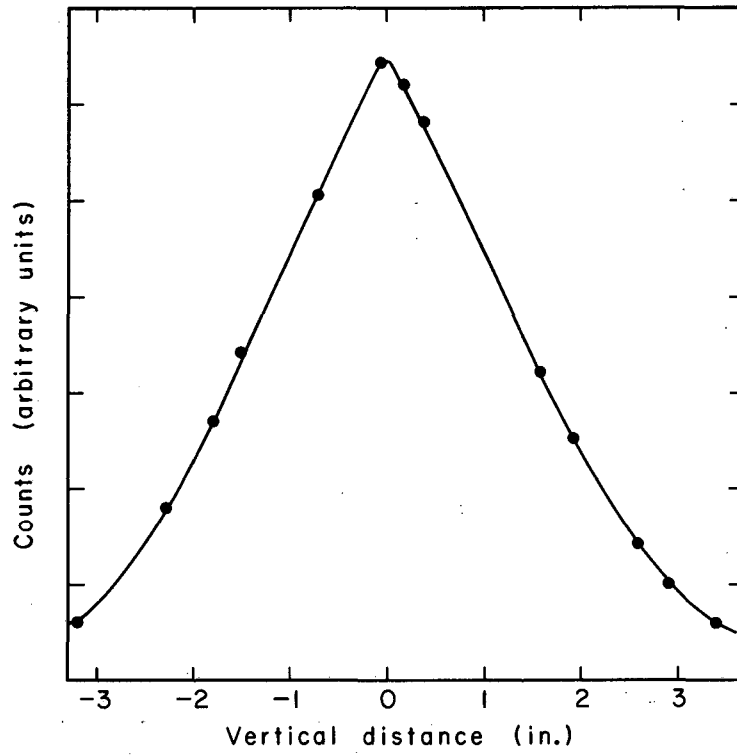
As a beam of charged particles passes through matter, collisions reduce the energies of the particles, and scattering changes their directions, and the eventual result of both processes is to remove particles from the beam. Consequently, the number of particles (or intensity) tends to decrease as the thickness of absorber increases. This particle loss is an extremely important consideration, since the dose available at the Bragg peak depends in part, on the intensity.

At low energies, the number of heavy particles lost from the beam is negligible, and virtually all the particles persist to the end of their range. An integral range curve for these particles has an initial slope of zero that extends out to the range of the particles, at which point there is a gradual slope that depends on the inherent statistical fluctuation in the energy-loss process. At the higher energies, inelastic nuclear collisions become important and the loss of particles from these collisions can become appreciable. In this case, the particle integral range curve has a definite slope. As an example: with



MU-34175

Fig. 4. Horizontal beam profile, taken at the position of the monitor chamber.



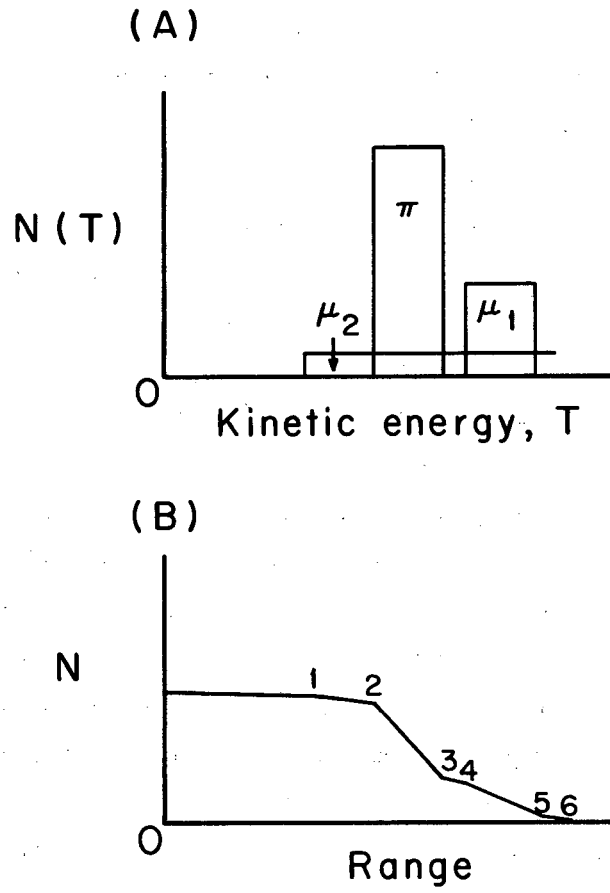
MU-34176

Fig. 5. Vertical beam profile, taken at the position of the monitor chamber.

300-MeV protons stopped in water, there is a loss of approximately 33% of the original particles from the beam before the end of their range.³⁵ In order to assess this problem of particle losses in the beam for π mesons, the net penetration of π mesons as expressed by the integral range curve was investigated. A determination of the average energy, energy spread, and degree of muon contamination was also made by this integral range method. A theoretical pion-beam energy distribution and its resultant integral range curve are shown in Fig. 6. In part A of this figure the beam energy distribution has been broken down into three components. The greatest contribution comes from the pion portion; the other two components represent the muons. One of the muons components, designated μ_1 , results from the decay of pions before the beam reaches the bending magnet and thus consists of only those muons whose range in momentum is the same as the pions. The remaining muon component represents the pions decaying after the bending magnet, and therefore has a much wider momentum spread. The extent to which the muon components are important depends upon the particular experimental setup and the distance of particle travel involved.

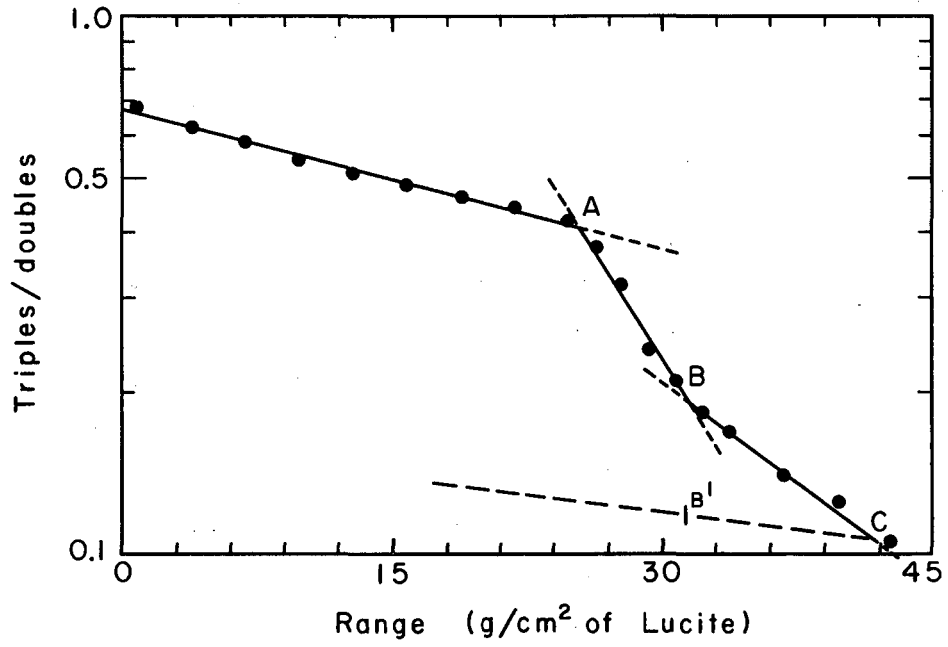
The integral range curve that would result from this particular pion beam is shown in part B of Fig. 6. The six breaks in the curve that should theoretically result from each of these components are indicated on the integral range curve.

An actual integral range curve was obtained by measuring the transmission of the beam as a function of Lucite absorber thickness. The results of this measurement are discussed in Chapter IV. One can readily note that not all the breaks indicated in the idealized curve of Fig 6 are shown in the actual integral range curve (Fig. 7). One of the factors contributing to this difference is that the energy distributions of the beam components are not actually rectangular, but rounded. Consequently the observed breaks are not distinct. Still another factor that affects the curve to varying degrees is the electron background



MU-34177

Fig. 6. Theoretical pion and muon energy distributions in a pion beam (A), and the resulting integral range curve (B).



MU-34178

Fig. 7. Integral range curve.

that may be present. The main source of these multiple-scattered electrons in the beam is the decay of π^0 produced in bombardment of the Be target with protons into two γ rays of approximately 70 MeV each, which give rise to an electron-positron pair. The electron whose momentum corresponds to that of the pions is then passed through the magnet system and may give rise to electron showers, depending upon the type and thickness of absorber.

Three breaks in the actual curve can be clearly distinguished, as shown in Fig. 7. Break A corresponds to idealized break 2 (in Fig. 6) that is, the break between the pion absorption loss curve and actual stopping of pions. Pions are stopped between A and B. The average pion energy is determined by taking the pion ranges at points A and B found from range tables.³⁶ The spread in the pion energy is half the difference between these two energies, after a small correction is made to this difference for range straggling.³⁷ Break B was identified with idealized breaks 3 and 4 and the beginning of the momentum-analyzed muon region. As was already pointed out, these muons result mainly from pion decays before the beam reaches the bending magnet, and therefore have the same momentum range as the pions. In order to obtain the fraction of muons present in the pion beam one must first determine the electron background at point B. Break C, corresponding to idealized breaks 5 and 6, designates the end of the muons and beginning of the electron shower tail. Point B', which is roughly the electron contribution to the measurement made at point B, is then ascertained by linearly extrapolating the electron background back to the range of point B. The difference between the fractions of the incident beam at point B and at point B' represents the fraction of muons in the beam with an energy greater than that corresponding to the muon range at point B. The complex nature of the electron-shower formation and the complexity in the interaction processes involved suggest that a simple linear extrapolation of the electron-shower tail of the range curve back to zero range, using measured

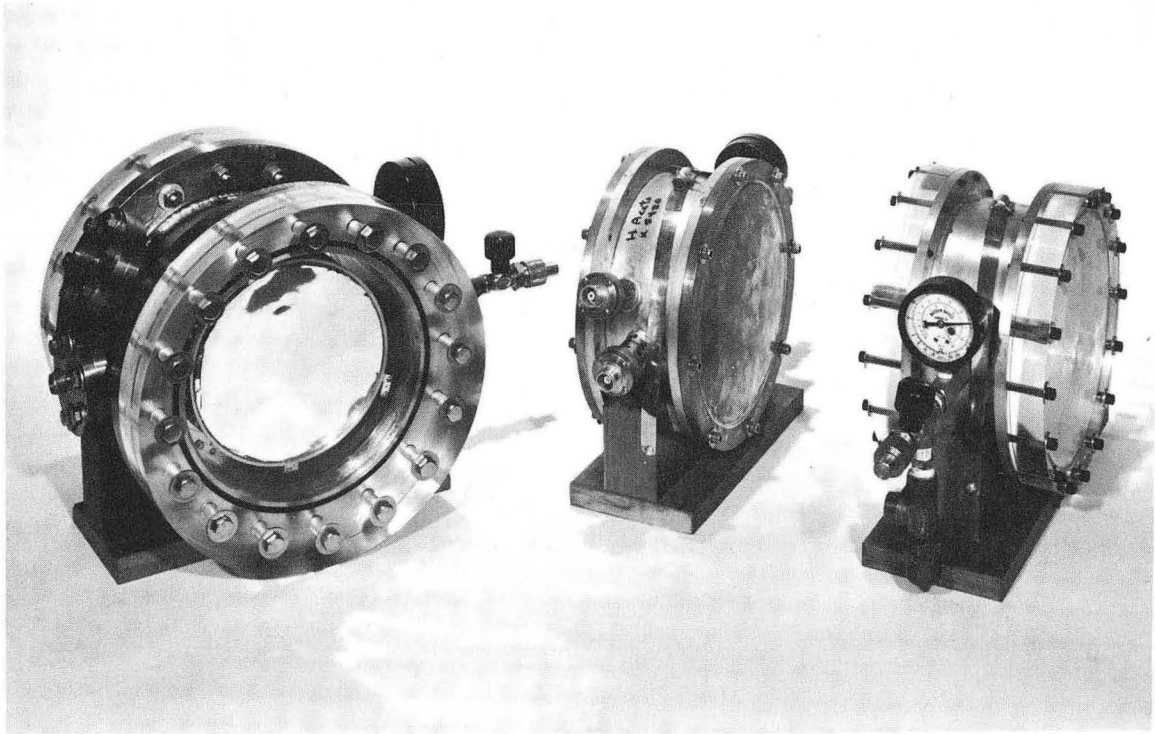
shower curves, gives a completely unsatisfactory result. Particularly in dose measurements with the ionization chamber, it is important to know with reasonable accuracy the fraction of the ionization measured that is due to electrons at the various depths in the absorber.

In a later experiment the electron contamination of the beam will be measured directly as a function of absorber thickness by use of a velocity-sensitive gas Cerenkov counter.³⁸ This gas Cerenkov counter, filled with sulfur hexafluoride, has a threshold value of $\beta = 0.99$. Therefore, only the electrons give a signal in the counter, since β for the pions and muons is considerably below this value.

B. Detection Techniques

1. Ionization Chambers

Intensity measurements were obtained by using 7-inch-diameter parallel-plate ionization chambers, as shown in Fig. 8. The chambers were designed with two high-voltage foils and a collector foil in the center, each of 2-mil aluminum, functioning as electrodes placed perpendicular to the beam. This arrangement of the collection electrode between the high-voltage electrodes eliminates a potential source of error arising from ions collected on the back of the collection electrodes. Various electrode spacings, gas fillings, and gas filling pressures were used in the different chambers, depending upon their specific functions. (See Table I.) A chamber with high-voltage electrode spacing of 2 inches, chamber window thickness of 5 mils, and A-CO₂ gas filling pressure of 2 psi above atmospheric was used as a beam monitor. This chamber will be referred to in further discussion as a low-pressure chamber. Ionization measurements as a function of absorber thickness were first made with a second chamber which was identical to the beam monitor. Later measurements utilized a detector which was also identical to the monitor except for its nitrogen gas filling. Two high-pressure chambers with high-voltage electrode spacings of 4 inches and maximum operating nitrogen gas



ZN-4306

Fig. 8. Ionization chambers.

Table I. Ionization chambers used in π^- -meson experiments.

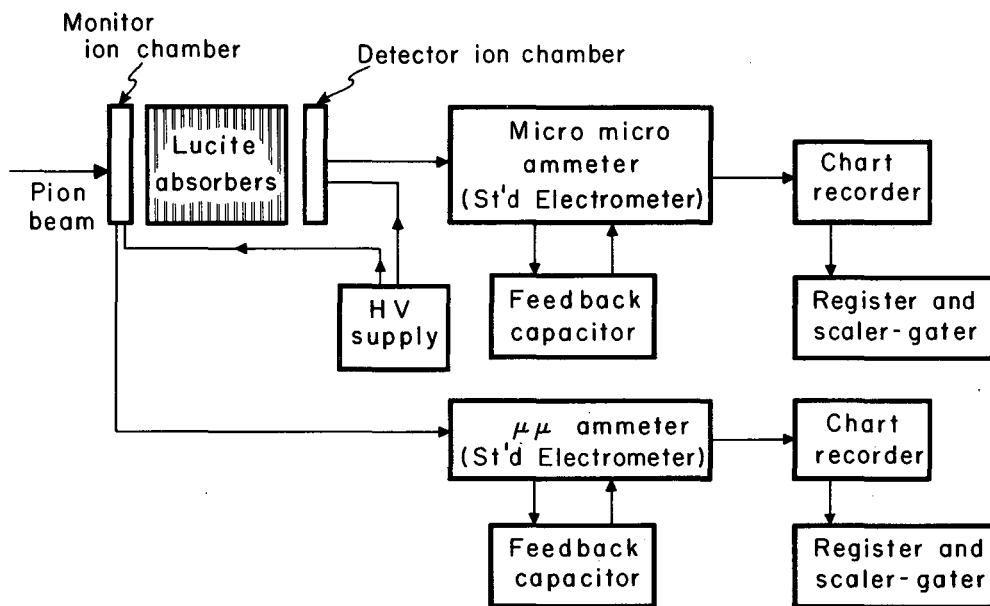
Chamber type number	Gas filling	Max. gas filling pressure (psi)	Distance between HV electrodes (inches)	Window material	Window thickness (mils)
1	A-CO ₂	16.7	2	Cu	5
2	N ₂	16.7	2	Cu	5
3	N ₂	219.7	4	Cu	851
4	N ₂	219.7	4	Lucite	1500

pressures of 6 and 15 atmospheres above atmospheric pressure were also used as detectors. (The window thickness of different materials required for the containment of the gas under these elevated gas pressures complied with safety code specification.) The charge collected in the ionization chamber is integrated by a capacitor, and the potential across the capacitor is measured with a standard integrating electrometer which is fed to an integrator timer system as shown in the block diagram of Fig. 9.

Recombination of positive and negative ions before they reach the high-voltage collection electrodes may present a serious problem in ionization-chamber measurements. However, the beam intensities observed in these experiments were quite moderate, and since the rate of recombination of ions is generally proportional to the density of ions of both signs, recombination losses were not considered to be a serious problem here. Nevertheless, saturation curves were plotted, for each chamber, of the ionization current as a function of the collection voltage for a given beam intensity. A typical saturation curve is shown in Fig. 10. At voltages sufficiently high to collect nearly all the ions produced, the curve reaches a plateau and the collection efficiency is very close to 100%. The operating voltages were chosen so that they were well within this plateau region. These experimental results for the collection efficiency were verified by calculation using the method of Boag, and by substituting the instantaneous intensity for the time-average ionization-chamber intensity measurement.³⁹

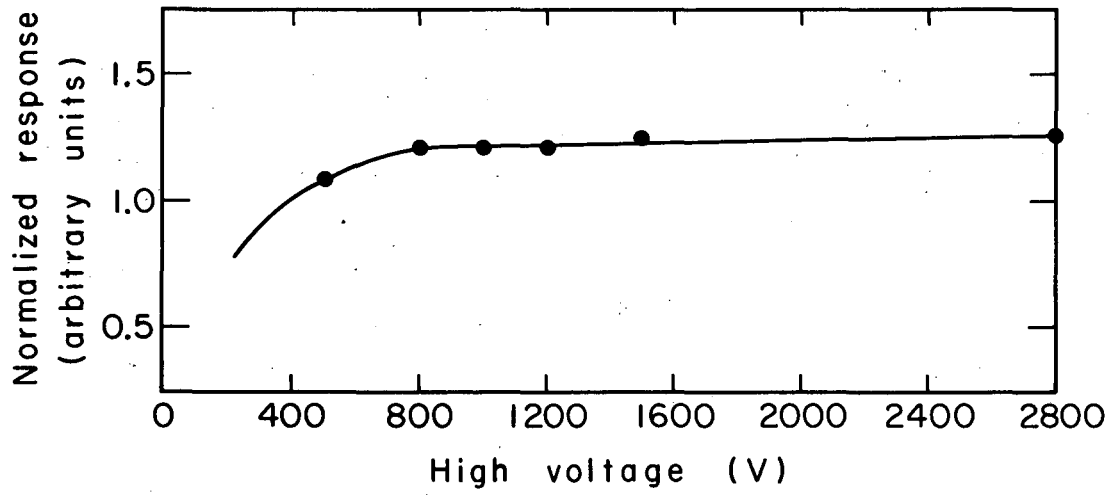
2. Scintillation Detectors

Plastic scintillation counters made of a solid solution of terphenyl in polystyrene were used in measurements of the integral range and beam profile. The passage of charged particles through these counters results in energy losses mainly by excitation and ionization of the atoms or molecules in the crystal. The subsequent electronic transitions are accompanied by the emission of light quanta,



MU-34179

Fig. 9. Ionization chamber - block diagram.



MU-34180

Fig. 10. Typical saturation curve.

which are then allowed to strike the photocathode of an optically coupled photomultiplier tube.

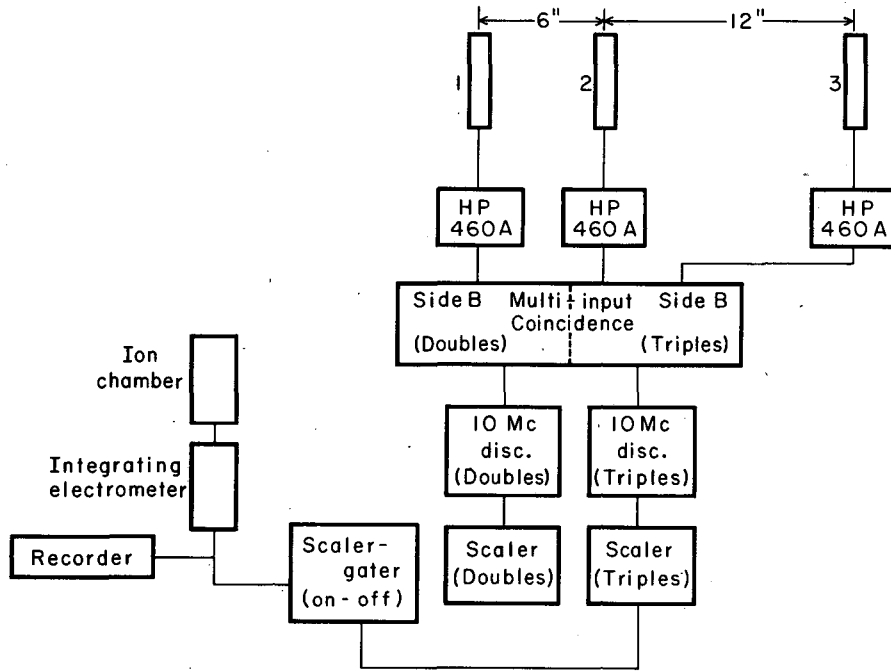
a. Integral Range Apparatus

The integral range apparatus consisted of three $4 \times 4 \times 1/8$ -inch plastic scintillators operating as particle counters. The light from the plastic scintillators was viewed with RCA 6510A photomultiplier tubes. Aluminum (Alzak) light guides were used to guide the light to the phototube. The positions of the counters and the associated equipment are shown in Fig. 11. The signal from the photomultiplier is amplified by Hewlett-Packard 460A wideband amplifiers and is then fed into a multi-input coincidence circuit.

The output pulses of the coincidence circuit are fed into 10-Mc discriminator units that in turn drive conventional scaling units. The resolving time of the system was of the order of 4 nanoseconds. With the detectors in such close proximity to each other it is not necessary to use delay times for the pulses produced by a single particle in the different counters, since it would take less than 2 nsec for the pions used in this experiment to traverse all the counters. However, the coincidence method was useful here in minimizing the number of accidental counts. The front two monitor counters were operated in double coincidence, thus minimizing the number of accidental counts. The double coincidence counts obtained from these counters served to define the actual beam intensity at zero absorber thickness, including the beam contaminants. A variable absorber was placed between the second and third counters and the first two counters were connected in triple coincidence with the third. A transmission-type measurement is then made of the beam intensity as a function of absorber thickness. A plot of the ratio of triple coincidences over double ones versus absorber thickness gives an integral range curve.

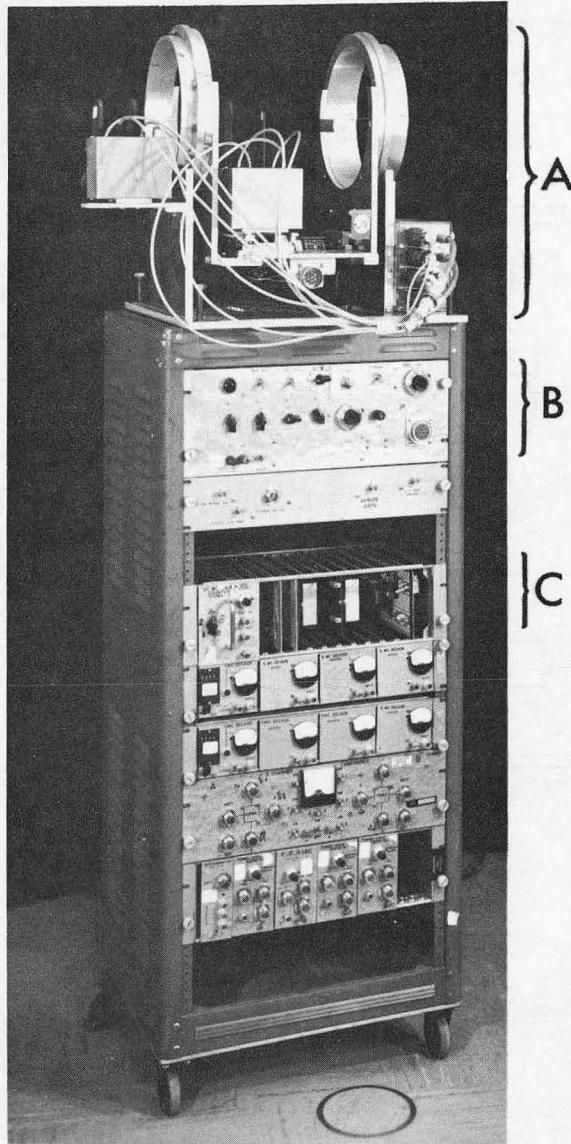
b. Beam Profile Apparatus

Figures 12 and 13 show the mechanical construction and block diagram of the associated electronics of the beam-profile detector. Two 2-inch monitor counters, in double coincidence, mounted on the



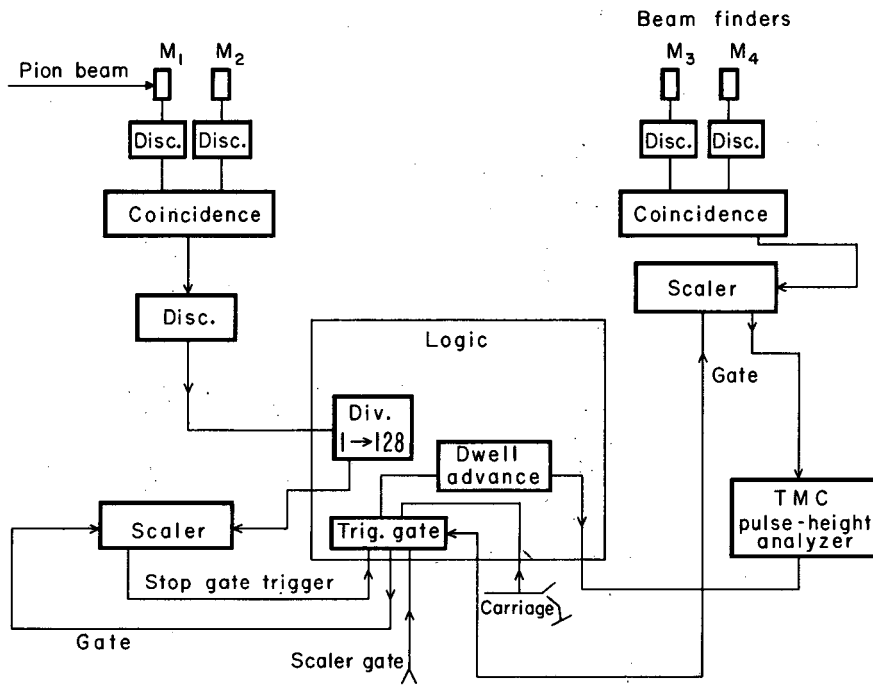
MU-34181

Fig. 11. Integral range block diagram.



ZN-3772

Fig. 12. Photograph of beam profile counter.



MU-34182

Fig. 13. Profile counter block diagram.

axis of rotation of a pair of cylinders which are aligned with the central axis of the beams, exhibit a counting rate which is proportional to the incident flux. A pair of "beam finder" scintillation counters measuring $3/8$ inch and 1.5 inches in diameter served to provide a double coincidence measurement of the intensity at points at various distances from the central axis, at right angles to the direction of the beam. The first (and smallest) counter functions to define the beam while the second is used to provide a double coincidence to minimize the number of accidental counts. All the scintillators were viewed by RCA 1P21 phototubes. The "beam finder" counters move over a 7-inch linear path, normal to the beam axis, taking a measurement every 0.1 inch. The number of beam-finder counts per unit incident flux at every 0.1 inch is consecutively stored in 70 channels of the TMC 400-channel pulse-height analyzer (PHA), and subsequently recorded on the associated printout mechanism. When 100 channels are used at a time, as many as four profiles may be stored at once and can be compared by overlapping the 400 channels of the PHA.

3. Semiconductor Detectors

Semiconductor devices are closely related to ionization chambers in their operation; like the ionization chamber, they respond to the passage of a heavy particle in proportion to the number of charge pairs produced (and collected) in its sensitive volume. Although the effective volume is very small, the solid silicon of which they are usually made is some 1850 times as dense as air at atmospheric pressure. Furthermore, the value of w , the energy necessary to produce an electron-hole pair, is only about 3.23 eV, or about 0.1 that necessary for an ion pair in air. The result is that energy resolution comparable to those in spectrometers using magnetic analysis can be obtained. Thus, per unit volume, the ionization yield will be, roughly, 18 000 times that in a chamber with a gas-filled cavity. In addition to their increased stopping power, these devices exhibit response times of the order of a few nanoseconds.

Two types of semiconductor particle detectors were used in the course of this study. Earliest measurements utilized a silicon surface-barrier detector. A surface-barrier detector consists of a rectifying junction formed at the surface of a silicon crystal between an evaporated gold layer and high-resistivity n-type silicon. These detectors were made to take advantage of the fact that the undamaged surface of a crystal can play the role of acceptor. Donor electrons from the interior of a phosphorus-doped n-type silicon crystal collect on the surface, establishing a high-resistivity region free of charge carriers near the crystal surface. A thin film of gold evaporated onto the surface increases the number of acceptor sites available and thereby widens the charge-carrier-free region.

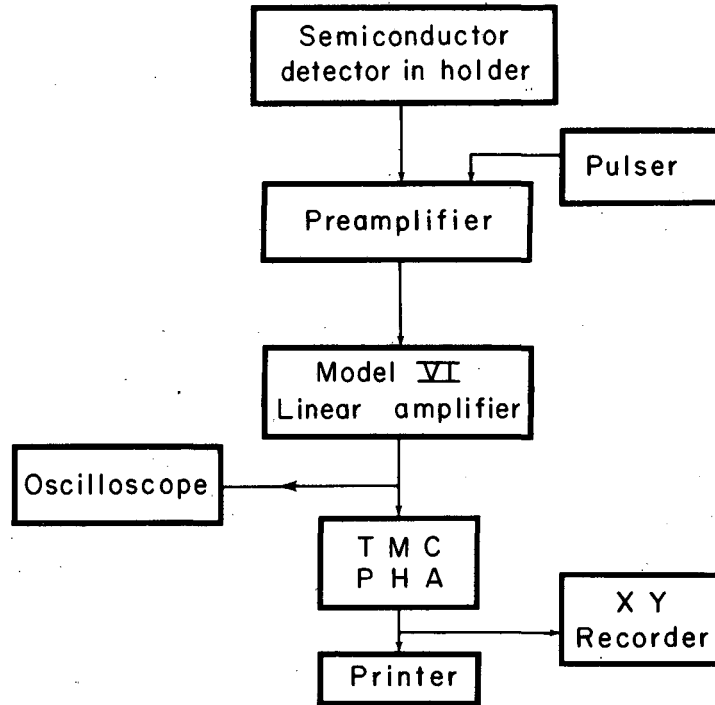
In principle, a surface-barrier detector operates in the following way: The gold-evaporated p region of the silicon conducts electricity only by motion of positive holes, or sites in the crystal lattice which are deficient in one electron that normally should be there. The n region, on the other hand, conducts by virtue of a surplus of electrons. If ohmic contacts are attached to the regions of the silicon and an electrical potential applied in a direction such as to attract both types of charge carriers toward the junction between the regions, a current flows across. If the polarity is reversed so that the charge carriers are attracted toward their own electrode and away from the junction, a "depletion layer" devoid of charge carriers is formed in the neighborhood of the junction, and no current normally flows across. The depth of this depletion layer (which is the sensitive region of the detector) is given by

$$d = 0.32 \sqrt{\rho V} \quad (\text{in microns}) \quad (4)$$

where ρ = resistivity (in ohm cm) of the n-type material,
 V = applied voltage.

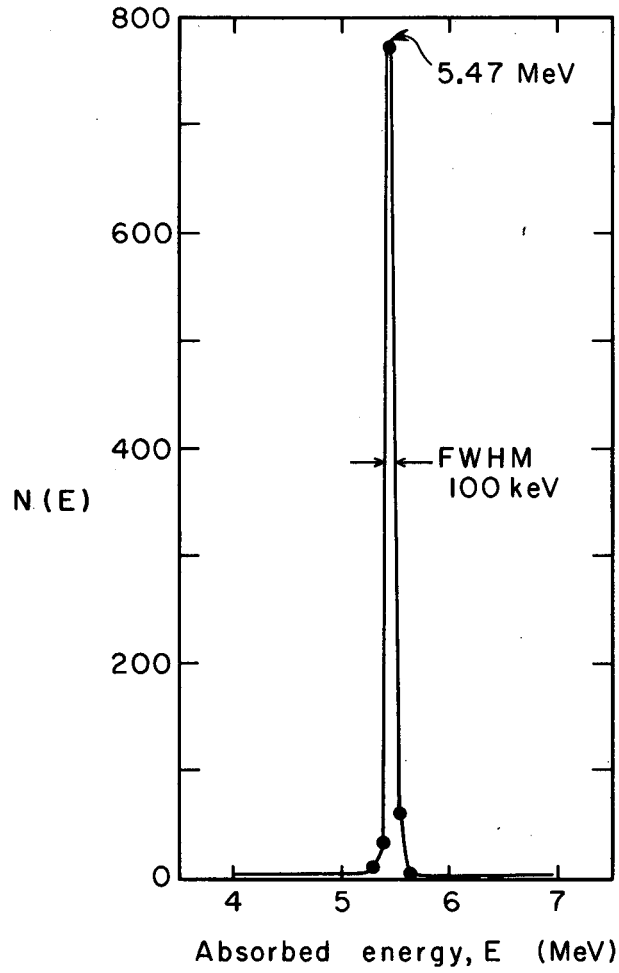
If the depletion layer is exposed to ionizing radiation, new pairs of charge carriers are generated there and are immediately collected by the potential across the layer, constituting an ionization current in the same sense as in a gaseous ionization chamber. A block diagram of the experimental arrangement is shown in Fig. 14. The signal from the detector entered a transistorized preamplifier and then went to a Model VI linear amplifier. The output pulse from the linear amplifier was fed into a TMC 400-channel pulse-height analyzer and the resultant pulse-height distribution was displayed by a printout recorder. In addition to providing amplification for the detector signal, the linear amplifier also serves as the high voltage source for the detector. Since the depth of the sensitive depletion layer increases as the square root of the applied voltage, the maximum available voltage of 100 volts was applied to the detector to produce a depletion layer of 200 microns. Calibration of the detector utilized an americium-241 source whose 5.477-MeV alpha particles were totally absorbed by the detector. For calibration purposes, pulse generator introduced, between the detector and preamplifier, a voltage comparable to the voltage output of the detector. In this way we obtained experimentally both a channel number and a pulse generator voltage corresponding to a 5.477-MeV pulse (see Fig. 15). The pulse generator was then used to verify the linear response of the electronic system over the anticipated range of energy measurements. Since the charge pulse created in a silicon semiconductor is directly proportional to the energy absorbed in the sensitive volume, and this energy absorbed is in turn directly proportional to the channel number and pulse generator setting, one can easily determine an unknown amount of energy absorbed by observing corresponding pulser settings to get the peak at the same channel number as that of the unknown energy absorbed.

The limited depth of depletion which in turn dictates the sensitive volume is a definite drawback to application of a surface-barrier type of detector to pion beams. Even with externally applied fields as



MU-34183

Fig. 14. Block diagram of semiconductor detector method.



MU-34184

Fig. 15. Response of surface barrier detector to totally absorbed 5.47 MeV.

high as 500 volts and the purest available silicon, the depth of the sensitive region is limited to a maximum of about 600μ .⁴⁰ This presents a serious problem in the application of these detectors to the dosimetry of high-energy pion beams, since they are relatively insensitive to the pions because so little energy is lost by the particles in traversing the shallow depletion layer. On the other hand, the detector is quite satisfactory for the detection of the low-energy heavy particles resulting from the negative-pion "star" events. Since the detector cannot bridge the large gap in linear energy transfers that is represented, it therefore detects one type of particle at the expense of another.

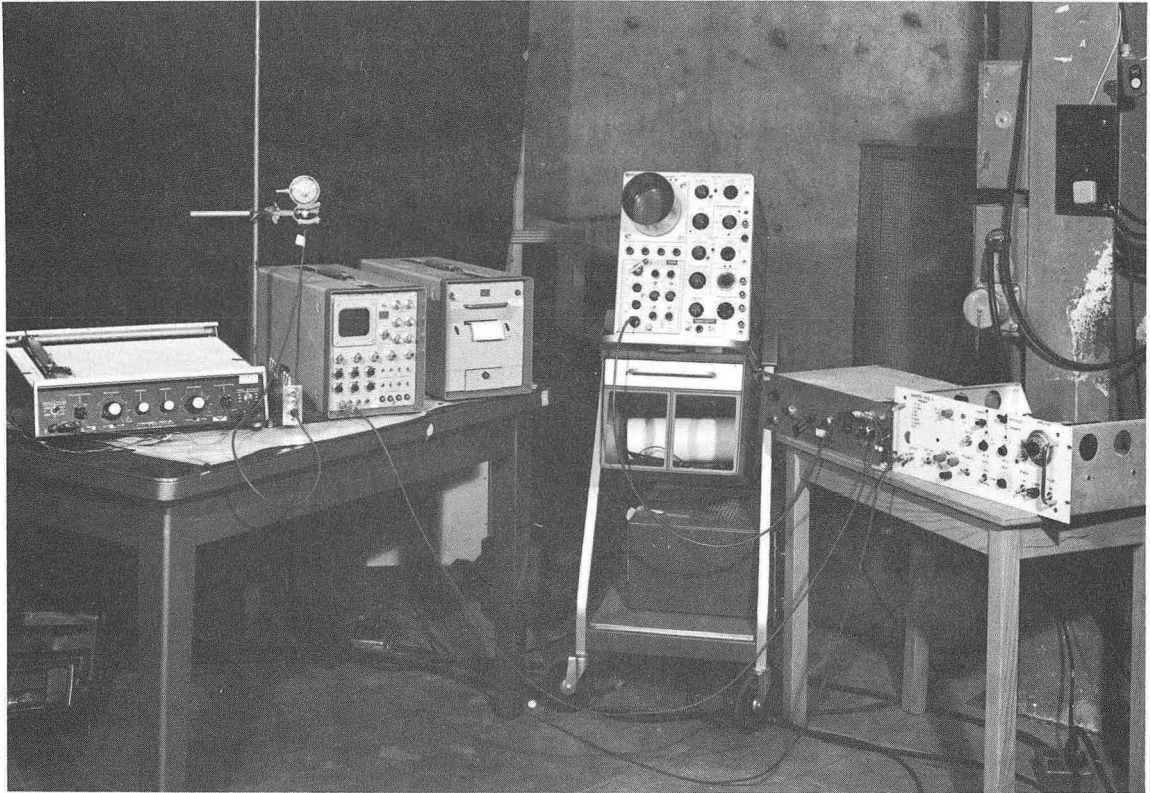
A considerable increase in the sensitive depletion region can be achieved by using a lithium-drifted solid-state device. This was the other type of semiconductor particle detector used in the experiment. Equation 4 shows that the depletion is directly proportional to the resistivity of the crystal, and very-high-resistivity material is necessary for thick detectors. Based on these considerations, the counters are made by diffusing lithium donor atoms into one face of a p-type silicon crystal. Lithium has a single outer-shell electron which acts as a donor impurity and creates an n-p surface junction. The lithium atoms do not fit themselves in the silicon crystal lattice, but remain interstitial and wander through the crystal lattice. When a voltage is applied to the crystal in the right direction, lithium atoms that have given up their valence electrons enter the p-type interior. There each ion eventually encounters a negatively charged acceptor site occupied by an electron, which it neutralizes or "compensates." The result is that all the acceptor sites within a certain zone (which is to be the sensitive depth) are eventually compensated, resulting in the formation of a zone of very-high-resistivity material. Sensitive depths as large as 6 mm have been achieved by drifting lithium from the front to the back face of the desired thickness of silicon.

Lithium-drifted detectors, with sensitive depths of 0.25, 1, 2, and 3 mm were used in this experiment. The detector is shown in Fig. 16 with its specially designed holder. The associated apparatus was identical to that for the surface-barrier detector.

Calibration of the detectors was performed by using Am²⁴¹ α particles and the internal-conversion electrons from Bi²⁰⁷ and Cs¹³⁷. The results for americium and bismuth are shown in Figs. 17 and 18. This calibration consisted of an accurate measurement of change in both the channel number and pulse-generator voltage per total energy absorbed (MeV), to confirm the linearity of the system. These results are shown in Fig. 19. Based on the calibration, the charge pulses associated with the absorption in silicon of 730-MeV protons and 940-MeV α particles from the 184-inch cyclotron, 40-MeV α particles from the Hilac, and 49-MeV protons from the 88-inch cyclotron were measured. The energies were degraded by placing absorbing material in the primary particle beam path and measurements were taken through the full range. The residual energies were calculated by using the tables of Williamson and Boujot⁴¹ and Rich and Madey³⁶. The results are discussed in Chapter 4.

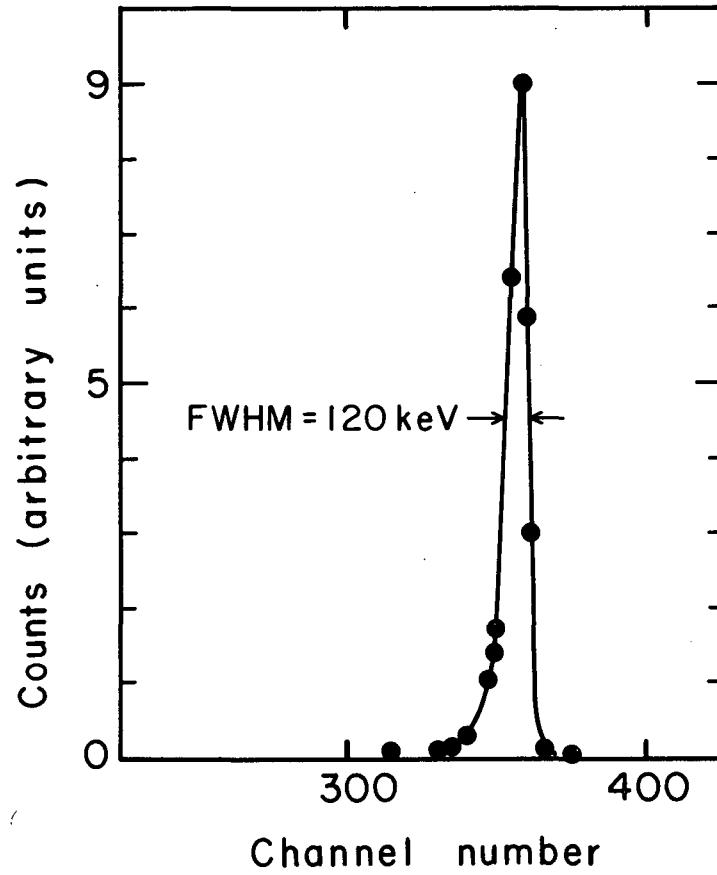
4. Thermoluminescence

When a thermoluminescent material is exposed to ionizing radiation, the electrons released in the ionization process are trapped at lattice imperfections throughout the crystal. These electrons remain trapped at room temperature but are released by thermal agitation at some elevated temperature. Upon release, they return to the ground state and emit light quanta in the process. The quantity of light emitted as the material is heated may be measured and related to the absorbed dose in the material by referring to a calibration curve of absorbed dose vs instrument response. However, since the competition between alternative energy-loss processes depends on the concentration of energy deposited along the track of the particle, at high LET,



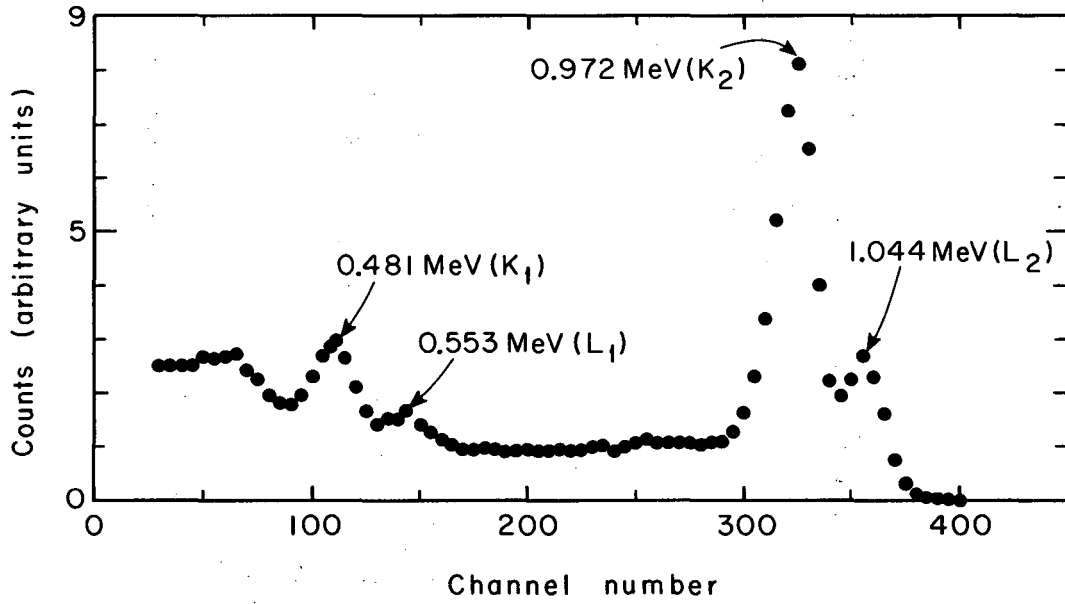
ZN-4307

Fig. 16. Lithium-drifted solid-state detector and its associated apparatus.



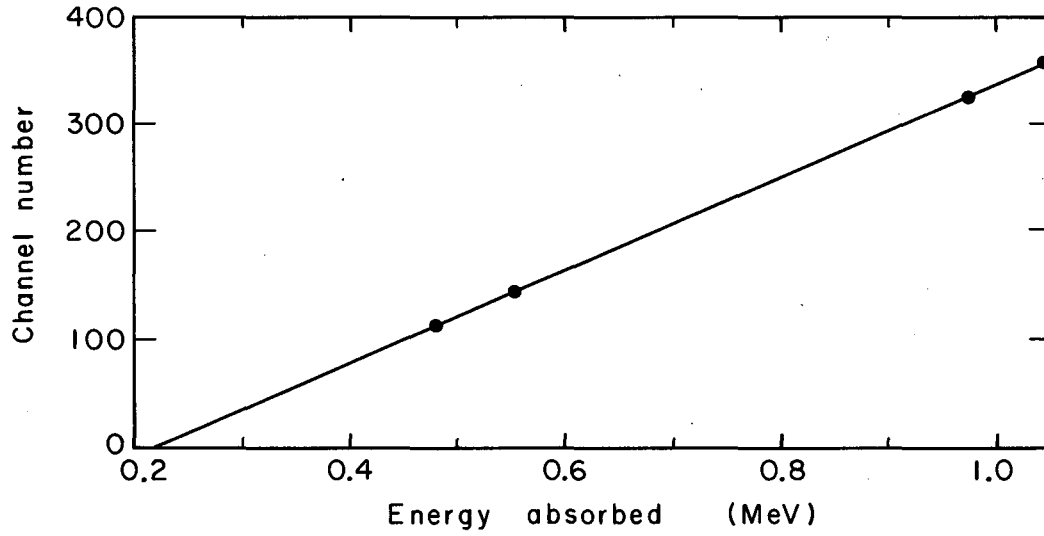
MU-34185

Fig. 17. Response of lithium-drifted detector to Am^{241} alpha particles (5.477 MeV)



MU-34186

Fig. 18. Response of lithium-drifted detector to Bi²⁰⁷ internal conversion electrons.



MU-34187

Fig. 19. Experimental check on linearity of system.

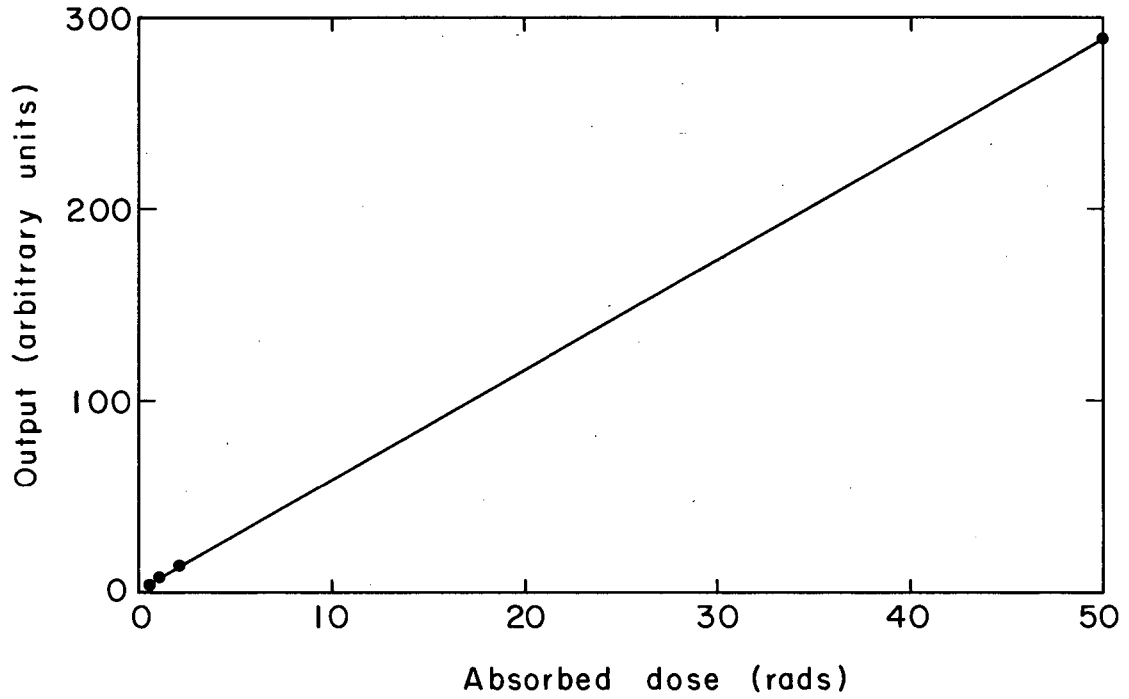
a correction must be applied to the detector response. For instance, at 100 KeV/ μ the detector response is decreased by approximately 75%.

The thermoluminescent phosphor used in this experiment was LiF powder. The thermoluminescence of LiF has an almost linear response to the quantity of low-LET radiation, as shown in Fig. 20. The dosimeter was in the form of a Lucite cylindrical capsule 1 inch high and 1/8 inch in diameter. To measure the thermoluminescence quantitatively after irradiation, the measured volume of powder in the capsule is placed on a planchet, and inserted into a readout system. (The use of the Con-Rad TLD System readout instrument was kindly made available to us by Eugene Tochilin and Norman Goldstein at USNRDL.) The planchet containing the LiF powder is positioned under a photomultiplier tube in the readout instrument by a sliding tray and heated to a temperature of about 250°C in a set period of time. The thermoluminescence intensity is integrated by collecting the photomultiplier current on a capacitor and then measuring the voltage of this capacitor with an electrometer voltmeter.

5. Photographic Film

Photographic film of various types was used for routine determination of position and size of the beam. The principal differences between these films and nuclear emulsions are the very high content of silver bromide in the nuclear emulsions (as much as four times the content in photographic film), the grain size, and the thickness of the emulsion. That sensitivity is a function of grain size is an important consideration in certain applications of the film.⁴² However, at the same time, this increased sensitivity with increasing grain size is achieved at the expense of the resolution. There is thus a conflict between greater response but poorer resolution on the one hand, and poorer response but greater resolution on the other.

Of course, in gross determinations of beam size and position this consideration is not of particular importance. Therefore, fast



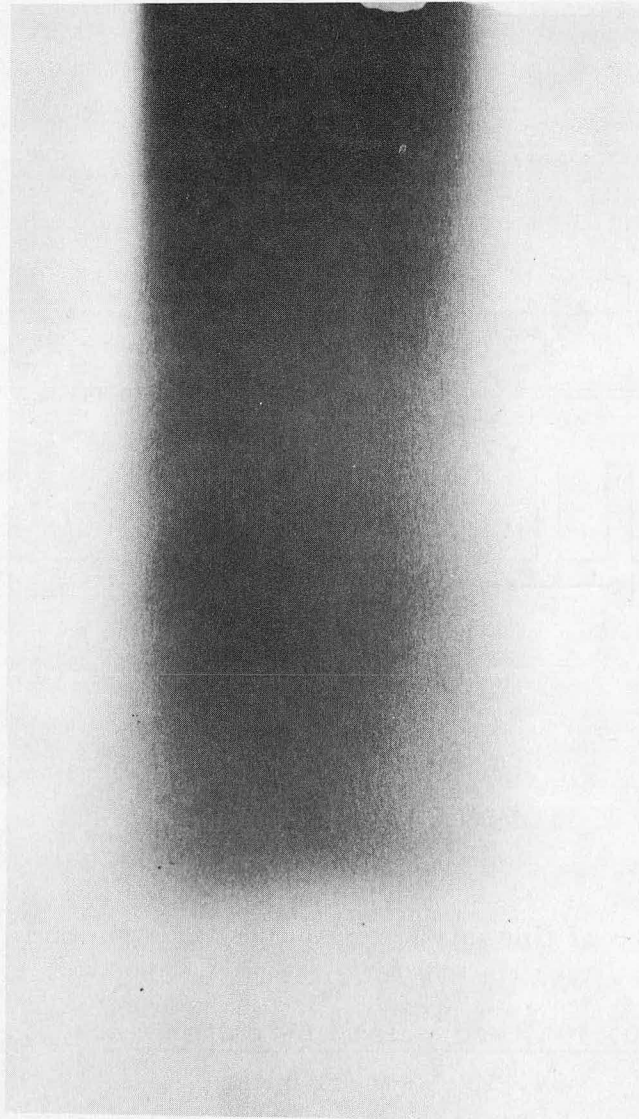
MU-34188

Fig. 20. Linear response of LiF dosimeter.

industrial x-ray film, type KK, was considered quite satisfactory. The film was positioned vertically with respect to the beam axis at various points to obtain a qualitative appraisal of both the size of incoming beam and the beam divergence (or increase in size) resulting from the traversal of absorber. However, to obtain an analysis of the finer structure of the beam cross section, one must use a much slower, fine-grained, less sensitive film. As we had more easily obtainable and somewhat more reliable information from the beam profile counter, this approach was not pursued. Some attempts were also made to secure a visual record of the Bragg curve on photographic film. The film was sandwiched between two slabs of Lucite and exposed to both π^- and π^+ meson beams for various periods. Figure 24 shows the response of Kodak type KK film to π^- pions. The beam is clearly visible, exhibiting the characteristic range of about 8 inches for the 90-MeV negative pions in the experiment, with the electron and muon component persisting beyond the range. However, as expected with fast films of poor resolution, there is no evidence of the Bragg peak or of the star events at the end of the range. An interesting qualitative observation of the beam, which is rather encouraging, is that the beam divergence does not seem to be very pronounced.

C. Counting Losses

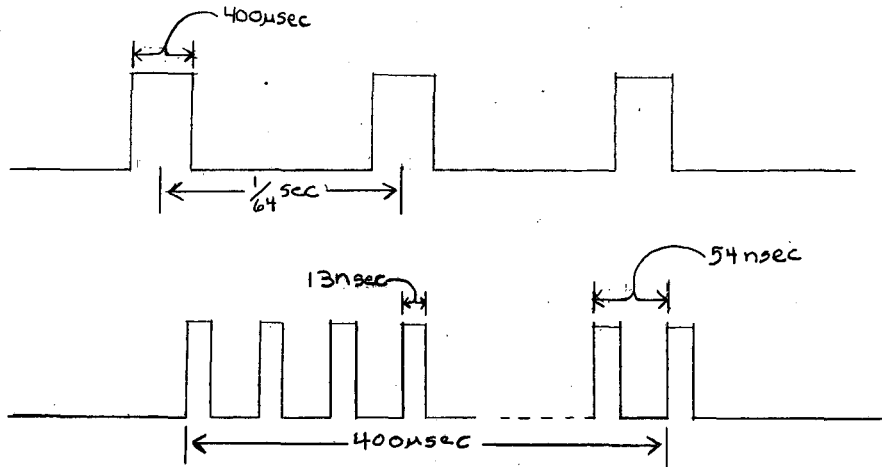
The pion beam exhibits a structure in time that reflects the accelerating characteristics of the 184-inch cyclotron. The cyclotron pulses 64 times per second, thus giving 64 coarse groups of pions per second. The mode of operation can be controlled so that these groups of pions can be spread out over either of two periods of time. The "short spill" mode spills the beam out over a period of approximately 400 μ sec. The auxiliary dee mechanism of the cyclotron makes it possible to spread each group of pions over a longer period of 8 msec. This "long spill" operation results in a cyclotron duty cycle (actual fraction of radiation time on) of about 51%, compared with 2.5% with



ZN-4301

Fig. 21. Response of Type KK photographic film to a 90-MeV π^- meson beam.

the "short spill." Each group of pions, regardless of their spill-out time, has a fine structure of pulses about 13 nsec long at a frequency of 1 per 54 nsec.



Short Spill

The number of fine-structure pulses per second is

$$\frac{400 \times 10^{-6} \text{ sec/pulse} \times 64 \text{ pulses/sec}}{54 \times 10^{-9} \text{ sec/rf pulse}} = 5 \times 10^5 \text{ rf pulse/sec.}$$

Since pions in the same rf pulse cannot be resolved electronically, the probability of having two pions in the same fine-structure pulse must be kept small for accurate measurements. Therefore, the beam intensity is limited to well below 10^5 pions per sec when a short-spill beam is used. Of course, the ionization chamber has an advantage here, since it records only the total charge collected, making the

problem of resolving two pions in the same fine-structure pulse unimportant. The problem of accidental counts and the necessity for limitation of intensity below a certain level was not as severe in this experiment, thanks to the auxiliary dee mechanism. With this device we have about 10^7 rf pulses/sec. Thus a beam intensity of 10^6 pions/sec can be counted without a terribly large probability of having two pions in the same fine-structure pulse. In fact, for such a beam the accidental counting losses amount to less than 10%, and for a beam intensity of about 2×10^5 pions/sec there are fewer than 2% accidentals.

III. THEORY

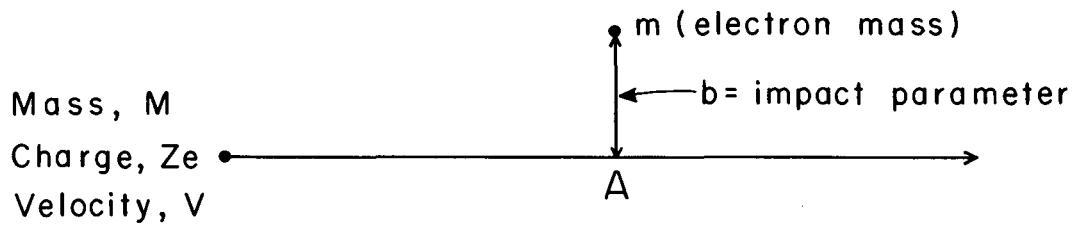
A. Interaction of Charged Particles with Matter

1. Energy Loss Formula

The theory of the stopping of charged particles by matter deals with the kinetic energy lost by the moving charge to the material through which it passes. All heavy charged particles, in their passage through matter, lose energy predominantly through ionization and excitation processes resulting from the interaction of the Coulomb field of the particle with those of the bound electrons or molecules in matter. A theoretical expression for this energy loss was first calculated by Bohr by means of nonrelativistic classical mechanics, assuming a Rutherford model of the atom.⁴³ The following approximate derivation follows closely that given by Fermi.⁴⁴ Consider an electron of mass m at a distance b (impact parameter) from the path of an incident particle having charge ze , mass m , and velocity v (see Fig. 22). Classically, the moving particle loses energy to an electron by imparting to it an impulse proportional to the strength of the Coulomb force between the two, and to the time during which this force acts. By symmetry the impulse ($F_{\parallel} dt$) parallel to the path is zero, since for each position of the particle to the left of A, yielding a forward contribution to the impulse, there is a position at equal distance to the right of A, giving an equal but opposite contribution. The impulse perpendicular to the path is then

$$I_{\perp} = F_{\perp} dt \approx (\text{electrostatic force}) (\text{time of collision}) \approx \frac{ze^2}{b^2} \times \frac{b}{v} \approx p_{el}, \quad (5)$$

where p_{el} is the momentum acquired by the electron. An exact calculation shows that I_{\perp} is actually equal to $2ze^2/bv$. We can express



MU-34189

Fig. 22. Diagram for theoretical expression of energy loss.

Eq. 5 in terms of energy if we square both sides and divide by $2m$. Then

$$E = \frac{P_{el}^2}{2m} = \frac{2z^2e^4}{b^2v^22m} \quad (6)$$

The number of electrons per cm of path in the range of impact parameters from b to $b+db$ is $2\pi n b db$, where n equals the number of electrons per cm^3 . Hence, the energy loss per cm to electrons in the range $(b, b+db)$ is

$$-dE(b) = \frac{2z^2e^4}{m^2v^2b^2} (2\pi n b db) = \frac{4\pi n z^2e^4}{m v^2} db \quad (7)$$

The complete rate of energy loss $\frac{dE}{dx}$ is obtained by integrating Eq. 7 between the limits b_{min} and b_{max} , which are the minimum and maximum values of b for which the above treatment of the energy transfer to the atomic electrons is valid. One thus finds

$$-\frac{dE}{dx} = \frac{4\pi n z^2e^4}{m v^2} \ln \frac{b_{max}}{b_{min}} \quad (8)$$

We now have the energy acquired by a single electron (which is also the energy lost by the particle to a single electron). Therefore, the energy loss per unit path length should be proportional to the number of target nuclei presented to the passing charged particle (electron density in the medium) and inversely proportional to the square of the velocity of the particle.

The strength of the Coulomb forces in an interaction according to Eq. 1 is a function of the impact parameter b , which is, roughly, the distance of closest approach of the incident particle to the orbital electron. The farther an electron is from the track of the particle, the smaller the impulse it can receive, and therefore, the smaller

the energy that can be transferred to it. If that energy is just less than the amount required to raise a K-electron to a higher level, no energy will be lost to K electrons at that distance. Somewhat farther away losses to L-electrons will become impossible, and so on. The tighter the binding of the atomic electrons (which incidentally increases with the atomic number) the shorter will be these "cutoff" distances, and the smaller the rate of energy loss. Consequently, the rate of energy loss should also show some dependence on atomic number, being less at higher atomic numbers.⁴⁵

Quantum-mechanically, the total inelastic-collision energy losses for charged particles (or the stopping power) is expressed by the Bethe formula,

$$\frac{dE}{dx} = \frac{4\pi z^2 e^4}{m v^2} NB \text{ (in ergs/cm)}, \quad (9)$$

in which e and m are the electronic charge and mass, ez and v are the charge and velocity of the incident particle, and N is the number of atoms per unit volume of stopping material. Basically, this formula for the stopping power differs from that of Bohr in its expression for the dimensionless multiplier B only. The dimensionless multiplier B is called the stopping number. The expression for B varies somewhat depending upon the energy region and particles involved. For heavy charged particles whose kinetic energy is of the order of magnitude of their rest mass, B has the value

$$B = Z \left[\ln \frac{2m v^2}{I} - \ln(1 - \beta^2) - \beta^2 - \frac{C}{Z} - \frac{\delta}{Z} \right], \quad (8)$$

where $\beta = v/c$, I is the mean value of all the ionization and excitation potentials of the absorbing atoms, and C/Z and δ are the shell correction and density correction, respectively. The mean excitation potential is a unique property of each material regardless of the

kind and speed of the incident particle. The energy I for many electron atoms is difficult to determine theoretically because information on the oscillator strengths, which is required for such an analysis, is scarce. Therefore, the value of I is generally determined empirically. An approximation has been developed by Bloch, using a Fermi-Thomas model of the atom, which predicts the mean excitation energy I to be proportional to Z , with the proportionality constant assuming a value equal to the ionization potential of atomic hydrogen. Thus we have $I = 13.6 Z$.⁴⁶ Despite this fundamental information, provided by theory, the main reliance is placed on experimental evaluation of I . Although there are some discrepancies in the values thus obtained, they result in much smaller discrepancies in the stopping power calculated from them, since I is a logarithmic function. The stopping-power formula holds only when $v \gg \mu_k$, where μ_k is the velocity of the orbital electrons in the k shell of the atoms in the stopping material. Then all electrons contribute equally to the energy loss. As the particle velocity is reduced, the contribution to energy loss by successive higher-shell electrons begins to fall off. Consequently, the mean excitation potential can no longer be defined as a velocity-independent parameter unless the necessary shell correction, C/Z , is introduced to account for the reduced contributions of those "nonparticipating electrons" with the velocity of the order of or greater than the velocity of the incident particle. The shell correction C/Z contributed by each electronic shell depends on the velocity ratio of the atomic electrons and the incident particles. Because of its logarithmic dependence, it modifies the stopping power by less than 1% at high energies, and by a few percent at most for the lower energies.⁴⁵

The relativistic correction term, $-\ln(1-\beta^2)-\beta^2$, causes the stopping power to increase with increasing energy of the incident

particle, at particle velocities close to the velocity of light. The first part of the term, $-\ln(1-\beta^2)$, arises from the increase of the maximum energy that can be transferred to the electron, while the last part, $-\beta^2$, is due to the enhancement of distant collisions. This enhancement is a consequence of the Lorentz contraction of the Coulomb field of the heavy particle which makes possible energy transfers to electrons at greater distances from the particle's path.

The remaining stopping-power correction to be considered is the density effect. This phenomenon relates the effect of the density and dielectric properties of the medium to the energy loss. Bethe's original analysis was based on the assumption that the atoms of the stopping medium were isolated from one another. It was later pointed out that the electric field of the incident particle at an atom far away from its path is decreased by the polarization of the intervening atoms, with the result that the energy losses by distant collisions are reduced.⁴⁷ Since the Lorentz contraction of the electric field of the moving particle makes distant collisions increasingly important at higher energies, this negative correction to the energy loss increases with increasing energy. Furthermore, this correction is rather small for heavy particles, even for relatively high energies. For instance, with 1000-MeV protons the effect is only of the order of 3% for iron.⁴⁸

The value for the stopping power is therefore obtained from the product of two factors. The factor in Eq. 8 (the factor in front of the brackets) is a monotonically decreasing function of the incident particle's velocity, while the second factor (in the brackets) is a logarithmic monotonically increasing function of the particle velocity. The second factor predominates at extremely high energies where the first factor approaches its limiting values ($v^2 \approx c^2$). In the intermediate energy range, the first factor's influence predominates

and causes the stopping power to decrease with increasing energy of the incident particle. The formula shows a decrease in energy loss as the particle velocity continues to increase, with a minimum occurring at an energy of about twice the particle rest mass energy. After the minimum the second factor predominates, as has already been noted, and the energy loss rises logarithmically with particle energy. As the velocity of the particle decreases, the first factor predicts an increase in rate of energy loss. As the particle velocity continues to decrease and approaches a velocity comparable to the orbital electron velocity, the gradual charge neutralization begins to dominate the velocity dependence, and the electronic stopping power goes through a maximum and then declines to zero. Unfortunately, there is no satisfactory theoretical expression for the rate of energy loss in this region. This information must be gained experimentally. In this energy region (≈ 7 keV for mesons) the average energy loss per unit path length from elastic nuclear collisions steadily increases to a maximum value and then it also declines to zero. Of course, the velocity region of interest here is relatively small and the energy available is quite insignificant. However, when dealing with heavy ions of increasing atomic number, such as argon, there is an expansion of the velocity region in which charge variation is important. In this case, such variations may influence the energy-loss process to a much greater extent.

The discussion thus far has been limited to the interaction of heavy particles with separate atoms. The treatment of a solid or liquid material as an aggregate of separate atoms interacting with the incident particle and with one another is expressed by the approximate "additivity rule" of Bragg. According to this rule, the stopping power for compounds and mixtures is approximately an average of the stopping powers of the constituent elements, weighted in proportion to the fraction by weight of each element. This approach

disregards chemical bonds and other aggregation properties of the material that modify the stopping power through changes of the spectrum of excited levels and through the density effect. Thompson made an experimental study to determine the validity of the additivity rule.⁴⁹ He reported small deviations from strict additivity; they were within 1% except for hydrogenous compounds, for which the deviations were up to about 2%. He also noted that these departures decreased rapidly with increasing atomic number.

The stopping power in a medium is of most fundamental value when it is expressed in MeV/g/cm^2 , which is independent of the actual density and physical state. This quantity is defined as the mass stopping power, $-\frac{1}{\rho} \frac{dE}{dx}$, where ρ is the density of the material. If the ionization losses were exactly proportional to the density of the absorber, then the mass stopping power for a given particle in different media would not vary. But $-\frac{1}{\rho} \frac{dE}{dx}$ depends on two other factors: (a) the number of electrons per g is less for heavier elements, (b) the ionization potential appearing in the logarithmic term in Eq. 8 is a function of the Z of the material. For example, the effective number of electrons per gram of tissue is 1.1% less than that for water. This means that for identical particle velocities, the mass stopping power of tissue is 1.1% less than that of water. In general, the mass stopping power decreases with increasing Z . This relative effectiveness in stopping particles by different media is expressed by the relative mass stopping power, S_m . Values of S_m can be calculated for particles of velocity v by the formula

$$S_m = \frac{Z_1 N_1}{Z_2 N_2} \times \frac{\ln 2 m v^2 - \ln I_1}{\ln 2 m v^2 - \ln I_2}, \quad (11)$$

where $Z_1 N_1 / Z_2 N_2$ is the ratio of the number of effective electrons per g in the two media, and I_1 and I_2 are their mean excitation

potentials. The variation of relative mass stopping power is a function of the energy of the incident particle.

The theoretical stopping-power formula can be quite useful in determining the range of heavy-particle beams of various energies. Such range-energy relations, $R(E)$, and their degree of agreement with these published values serve as a worthwhile check of experimental results. Since $-\frac{dE}{dx}$ is defined as the mean energy loss per unit path length, it follows that the mean path length, or range, is given by

$$R(E) = \int_0^{E_0} dE / -\left(\frac{dE}{dx}\right) \quad (12)$$

Although the values for the stopping power at very low energies is quite uncertain, integration over the complete energy range causes little uncertainty in $R(E_0)$ for fast charged particles, since the values for dE/dx are certainly very large in the low-energy region and therefore contribute little to the integral.

The energy loss of heavy charged particles in matter is a statistical phenomenon, since any given particle loses its energy in small but finite amounts, involving a large but finite number of independent collisions. Because of the statistical fluctuation in the energy-loss process, individual particles starting with the same velocity at the same point may follow different paths and at any given depth of penetration are distributed in energy, range, and lateral displacement from the projection of their initially common path. These fluctuation effects are known as "straggling." Because of this effect, different particles starting under identical conditions have tracks of different lengths, and the range formula above represents only a mean value of these lengths. For heavy particles this mean range is a useful quantity, since the straggling distributions are approximately Gaussian, with their center occurring at the mean range.

However, fractional energy transfers in electronic inelastic collisions are quite different depending upon whether the loss is by an electron on the one hand, or by a heavy charged particle on the other. For electrons the energy loss in a single collision may be as much as one-half of the incident electron energy, compared with the maximum fractional energy loss per collision for protons and π mesons of 0.227%, and 1.47%, respectively. As a result of these larger losses by electrons, an inherent straggling of energy is introduced by their passing through matter which is relatively much greater than that for heavy particles, and whose distribution is far from being Gaussian. Furthermore, this asymmetric distribution is not limited to electrons, for it must also be considered when elastic nuclear collisions in the energy-loss process are relatively important or when one deals with short sections of path over which the total energy loss is not much larger than the maximum fractional energy loss. Thus the difference between the mean and the most probable range (and energy loss) may be considerable.⁵¹ We have already noted that elastic nuclear collisions are not of any importance for our purposes. However, the short effective path length in ionization chambers deserves some attention.

Since the shell and density corrections are not considered to be significant, the Bethe formula for the average energy loss may be written as

$$-\frac{1}{\rho} \frac{dE}{dx} = \frac{2\pi z^2 e^4 NZ}{\rho m v^2} \left[\ln \frac{2 m v^2 Q_{\max}}{(1-\beta^2) I^2} - 2\beta^2 \right], \quad (13)$$

where Q_{\max} is the maximum possible energy transfer to an orbital electron in a single collision, $Q_{\max} = \frac{2 m v^2}{1-\beta^2}$. On the other hand,

the result for the probable energy loss is

$$-\frac{1}{\rho} \frac{dE}{dx} = \frac{2\pi z^2 e^4 NZ}{\rho mv^2} \left[\ln \frac{mv^2 W_1}{I^2(1-\beta^2)} - \beta^2 + K \right], \quad (14)$$

where W_1 is that individual energy loss which occurs on the average just once in the distance X (in g/cm^2) over which the energy loss is observed,

$$W_1 = \frac{2z^2 e^4 NZX}{\rho mv^2},$$

and the constant term, K , represents the most probable loss from energy transfer of order W_1 . Landau⁴⁹ gives $K = 0.37$. If the probable loss is denoted by ΔE_p , Eq. 14 can be expressed as

$$\Delta E_p = W_1 \left[\ln \frac{mv^2 W_1}{(1-\beta^2)I^2} - \beta^2 + 0.37 \right]. \quad (15)$$

A simple criterion has been suggested to decide whether, for any given conditions, probable and mean energy loss differ significantly.⁴⁸ It is only necessary to compare the energy W_1 with the maximum energy, Q_{max} , that the incident particle can transfer to the secondary electron. If $W_1 < Q_{\text{max}}$, the probable energy-loss formula (Eq. 15) should be used; if $W_1 > Q_{\text{max}}$, the most probable energy loss agrees essentially with the average energy-loss formula. This effect is considered further in Chapter IV.

In addition to electronic inelastic and elastic nuclear collisions, multiple scattering may also contribute to experimental straggling. The lateral displacement of the beam particles due to multiple Coulomb scattering is particularly important for electrons, resulting in the gradual divergence of an initially parallel beam and concomitant reduction in the net penetration of the particles by causing their tracks to depart from straight lines. Since the π meson has a rest mass which is greater than that of the electron but less than that of

the proton, the degree of scattering it experiences and amount of straggling that results should be much less than for the electron but greater than for the proton.

2. Linear Energy Transfer

A quantity closely allied to the stopping power is the linear energy transfer (LET). The LET differs from the stopping power in that it is concerned with the transfer of energy to the material, rather than with particle energy loss. That is, the stopping power of charged particles when passing through matter consists of ionization, excitation, production of bremsstrahlung, and other less important effects, such as Cerenkov radiation. The LET refers to those cases of energy loss in which the energy supplied by the particles remains in the near vicinity of the track, such as in ionization and excitation (including delta rays). This is significant when the biological effect of the radiation is being considered, since biological effect has been found to depend on the distribution of energy loss along the particle track as well as on the total energy absorbed per gram. The LET may be inferred directly from the determination of the stopping power if one assumes that all the energy, including the delta rays, is locally absorbed. If it is considered that delta rays of more than a certain energy are not locally absorbed, energy transfers of more than this amount must be excluded from the calculation. In radiobiological practice, it will not generally be possible to use directly Bethe's LET values (or electronic stopping power), because there is no uniform particle energy. Even with monoenergetic radiation an energy spectrum (and thus a LET spectrum) results from the production of secondary radiation and from the degradation of primary radiation and its associated straggling. There is thus a distribution of LET values, and one must either calculate some sort of average value, derive the complete distribution, or rely on an experimental determination.

3. Bragg Curve

An experimental confirmation of the theoretical stopping power may be obtained by measuring the ionization produced as a result of the energy loss. The resultant relative distribution of total ionization along the path of a high-energy particle (specific ionization) is, in first approximation, the same as that of the rate of energy loss, $-dE/dx$. The two quantities are related absolutely through the value, w , of the average energy expended per ion pair (ip) produced, by the equation

$$-\frac{dE}{dx} = w \frac{dJ}{dx} \quad (16)$$

The specific ionization $\left(\frac{dJ}{dx}\right)$ is determined experimentally by taking the ratio of readings obtained from two ionization chambers, one of which is placed before and the other after a variable thickness of absorber. The result is a Bragg curve of average specific ionization (ip/cm) vs residual range, which is directly proportional to the charge of the particle and inversely proportional to the velocity. There are two distinct regions of interest in such a curve. As was already noted, the initial portion of the energy-loss pattern (and resultant ionization) is represented by a relatively broad flat plateau region which is followed by a rapid rise in ionization caused by the increasing energy loss with decreasing energy. As the particle velocity continues to decrease, the gradual charge neutralization begins to dominate the velocity dependence, and the specific ionization goes through a maximum and then extends to zero. This second region of the Bragg curve is the Bragg peak. Since the relative mass-stopping power of tissue compared with the chamber gas filling and the energy expended per ion pair in the gas are relatively constant over a broad range of energies, the peak-to-plateau ionization ratio can be readily converted to a tissue-dose ratio. This

ratio may represent an extreme depth-dose advantage, particularly in the treatment of deep-lying tumors of the body. It should be mentioned at this point that a Bragg curve of the average specific ionization differs in principle from curves of the specific ionization of an individual particle. The Bragg curve is an average over a large number of individual particles and therefore reflects the statistical nature of the energy-loss process. The range straggling results in a flattening and broadening of the Bragg peak and a distribution in actual ranges of the particles which is characterized by a long tail. Since a measurement of the average specific ionization is intimately connected with the absorbed dose and LET at the point of measurement, one may say that these parameters will be affected in the same way.

In many cases the high-energy secondary electrons escape from the ionization chamber or other detection device and dissipate a good part of their energy outside the chamber (or sensitive volume). This is an important consideration when one realizes that a considerable fraction of the ionization may be produced by delta rays. The energy loss detected in such devices is not the average energy loss, but that portion associated with individual energy losses that are less than a certain value T ; T is determined by the absorption and geometry of the chamber. In addition, unless these corrections are made, there will be poor agreement between the theoretical stopping power and the experimentally determined ionization pattern. The reason is that the Bethe formula is expressed in terms of the maximum energy transferrable, and experimentally only energy transfers below a fixed amount are measured. For the case in which the finite size of the counter is such that not all the secondary electron energy is deposited in the chamber, the correct expression for the theoretical average energy loss is obtained by substituting E_1 for Q_{\max} . Then Eq. 13 becomes

$$\left(-\frac{1}{\rho} \frac{dE}{dx} \right) = \frac{2\pi z^2 e^4}{mv^2} NZ \left[\ln \frac{2mv^2 E_1}{(1-\beta^2)I^2} - 2\beta^2 \right]. \quad (17)$$

For energy-loss measurements in a solid-state device the measurable energy transfers extend to Q_{\max} and therefore Eq. 13 is valid.

B. Meson Production

The two fundamental mechanisms for the production of π mesons are photon-nucleon collisions and nucleon-nucleon collisions. Since in the cyclotron the nucleon-nucleon mode is utilized, the discussion is limited to this process.

The production of meson quanta in nucleon-nucleon collisions (and the associated nuclear forces) may be compared with the production of light quanta in electron-nuclei or electron-electron collisions (and the electromagnetic or Coulomb forces). In the latter process the electron and nucleus each has a virtual photon field associated with it. The Coulomb interaction may be considered to be the consequence of the virtual emission and reabsorption (or exchange) of light quanta by the electrons and nucleus. In the electron-nuclei collision (ordinary bremsstrahlung) for instance, the electron, which has a virtual photon field associated with it, cannot radiate this field unless there is a transfer of momentum to another particle (or nucleus) such as takes place in the Coulomb interaction.

In a similar fashion, the forces in the nucleus holding the nucleons together may be accounted for by a continual exchange of quanta of energy (or virtual mesons).

The various types of meson exchanges between pairs of nucleons that give rise to these nuclear forces are schematically shown below.

- a. n-n forces resulting from exchange of neutral meson (mechanism same for p-p forces).

Initial state	Virtual processes	Final state
n_1	$n_1 \rightarrow n_1^1 + \pi^0$ (emission)	n_1^1
n_2	$\pi^0 + n_2 \rightarrow n_2^1$ (absorption)	n_2^1

- b. n-p and p-n forces resulting from exchange of charged meson.

Initial state	Virtual processes	Final state
n_1	$n_1 \rightarrow p_1 + \pi^-$ (emission of π^-)	p_1
p_2	$\pi^- + p_2 \rightarrow n_2$ (absorption of π^-)	n_2

p_1	$p_1 \rightarrow n_1 + \pi^+$ (emission of π^+)	n_1
n_2	$\pi^+ + n_2 \rightarrow p_2$ (absorption of π^+)	p_2

In meson production, there is an exchange of virtual mesons between interacting nucleons, and these virtual positive, negative, and neutral π mesons--which are believed to be associated with all nucleons--are thus converted simultaneously into π mesons. The term "virtual" is used to indicate that the emission and reabsorption take place so rapidly that it cannot be detected, as explained by Heisenberg's uncertainty principle.

McMillan and Teller⁵⁰ (using the Fermi gas model of the nucleus) have shown that if E is the incident kinetic energy of a nucleon, the threshold for π -meson production may be roughly estimated by

$$E_f = m_\pi c^2 + E_f + V, \quad (18)$$

where $m_\pi c^2$ = rest mass energy of π meson,

E_f = Fermi kinetic energy (≈ 25 MeV),

and

V = average potential energy of nucleon in the nucleus. For fairly light nuclei, in which $A \approx 2Z$, the value of V is approximately 33 MeV.

The maximum kinetic energy of the bound nucleons, or the Fermi kinetic energy, E_f , is given by

$$E_f = \frac{\pi^2}{2M} \frac{3N^{2/3}}{\pi\Omega}, \quad (19)$$

where N = number of neutrons or protons,

M = mass,

Ω = nuclear volume.

The same value is found for neutron and proton gas, namely

$E_f = 25$ MeV.

Thus, a nucleon must possess a kinetic energy in the laboratory system equal to $m_\pi c^2$ plus the binding energy of a nucleon in the nucleus ($V - E_f = 8$ MeV) in order to produce a π meson.⁵¹ The crude approximation for the threshold kinetic energy of π -meson production in beryllium is then on the order of 150 MeV. This approach assumes that the π meson is produced in a collision of the incident nucleon with one of the nucleons in the Fermi gas. Barkas has obtained an absolute threshold energy for the production of π mesons by treating the production process as if the entire target nucleus participates as a unit in the collision with the incident nucleon.⁵² Thus, if a particle (or incident nucleon) of mass M_1 is incident upon a nucleus of mass M_2 the threshold kinetic energy, T_t , is given by

$$T_t = \frac{(m_\pi c^2 + M_i)^2 - (M_1 + M_2)^2}{2 M_2}, \quad (20)$$

where the total final mass of the colliding particles, M_i , is approximated by $M_i = M_1 + M_2$, and $M_\pi c^2$ is the rest mass of the pion.

This approach indicates a threshold kinetic energy for a proton projectile on a beryllium target of about 155 MeV. As the size of the nucleus decreases, this threshold energy can be seen to generally increase to a maximum value for the hydrogen nucleus (which is essentially a free nucleon-nucleon collision) of approximately twice the pi-meson rest-mass energy. Unlike the proton of a hydrogen nucleus, a proton in a heavier nucleus is not completely at rest, but possesses energy of motion. The chief effect of this motion (and its resultant finite momentum) is to lower appreciably the threshold for meson production. It should be emphasized that this value is an absolute threshold. In practice, the lowest energies (or actual threshold) at which mesons are observed is generally higher than the above theoretical threshold, because the incident nucleon most likely does not interact with the target as a unit, but separately in collision with the individual nucleons of the target nucleus. This analysis is justified by the fact that even at the proton energies required for meson production, the associated deBroglie wave length of the incident nucleon is small compared with the range of nuclear forces. The threshold of the complex nucleus is then lowered from the free nucleon-nucleon threshold by the momentum distribution of the target nucleons in the nucleus to equal the actual threshold. The value for the actual threshold for protons on beryllium is about 180 MeV.⁵¹

In addition to its effect on the threshold for meson production, the finite nucleon momentum serves to markedly influence the excitation function and the angular distribution and energy spectra of

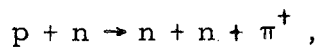
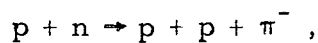
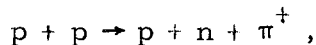
the produced mesons. The excitation function is an expression of the relative pion yield as a function of incident nucleon energy. In other words, it expresses the variation of cross section with the energy of the incident nucleon. This expression shows a steep positive slope (rapid increase) for π -meson production in nucleon-nucleon collisions above threshold with increasing incident nucleon energy.⁵³ Since the threshold energy is depressed to about $m_{\pi}c^2$ by the momentum distribution of the nucleon in the target nucleus (from about $2m_{\pi}c^2$ in free nucleon-nucleon collisions), the rapid variation should persist until the incident nucleon energy is at least $2 \times E_t$.

The pion yield at a certain incident-nucleon energy is further modified by the atomic number of the target material. Experimental studies have revealed that the relative cross sections for pion production vary approximately as the geometrical cross sections of the target nuclei.⁵⁴ However, further modification is introduced by the fact that the cross section for the interaction with nucleons of the π mesons that are produced is also close to geometrical. As a result, the produced meson may suffer a collision during the course of its traversal of the nucleus, and may not emerge from the nucleus. This interaction effect of the meson becomes increasingly more important for heavier nuclei, and therefore one observes a maximum in the production cross section as a function of target nuclei size which reflects this effect.

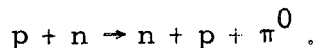
The mesons produced at energies above threshold have a continuous energy distribution extending from zero to the maximum allowable energy. The maximum kinetic energy is associated with pions emitted at 0° with respect to the incident nucleon, and it is roughly equal to the kinetic energy of the incident nucleon minus the threshold energy. With increasing angle, the angular distribution

(or differential energy spectra) shows a decrease in the maximum observable energy and a shift (to lower value) of the position of maximum in the distribution spectrum.⁵¹

Nucleonic production of mesons may be represented by interactions of the type



or

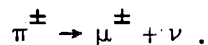


In each of the above equations, the high-energy incident nucleon experiences an inelastic collision with one of the nucleons in the nucleus, and a good deal of its energy (140 MeV) is utilized to convert virtual π mesons into free π mesons. At the same time, the conservation of charge is fulfilled. The p-p collision gives rise only to positive mesons, with either one of the colliding protons changing into a neutron. In contrast, the p-n collision may give rise to a positive meson (with the proton changing into a neutron) or a negative meson (with the neutron changing into a proton). Since light nuclei such as beryllium contain approximately equal numbers of protons and neutrons, one would expect the bombardment of these nuclei with protons to result in a π^+/π^- ratio considerably greater than one. Experimental results indicate that this conclusion is correct only for very large energies. At lower energies the exclusion principle and the Coulomb barrier serve to markedly alter the positive-to negative ratio.⁵¹

C. Meson Decay and Interactions

An important and characteristic property of π mesons is their instability. Positive and negative mesons exist as such for a very short time, as expressed by their mean lifetime of $\approx 2.6 \times 10^{-8}$ sec. It should be noted that this meson lifetime is for very low velocities and is generally referred to as the "rest" value. When the velocity is much higher, the lifetime is expanded significantly, through the effect of relativity, by the factor $1/(1-v^2/c^2)^{1/2}$. If τ is the mean life of the meson at rest, the apparent mean life of a meson moving with a velocity βc is $\tau/(1-\beta^2)^{1/2}$. The average distance traversed by the meson before it disintegrates is thus $d = \beta c \tau / (1-\beta^2)^{1/2}$. For a 100-MeV pion this distance equals about 35 feet. As has already been mentioned, this particular parameter is quite important in determining the extent of contamination of the desired π -meson beam. The lifetime of the π^0 meson is extremely small ($\approx 10^{-16}$ sec), and except for the electron contamination that it produces, it will not be dealt with any further.

The disintegration of a π meson is represented by



It has been shown that, if the disintegration reaction takes place while the meson is at rest, the average range of the muon in emulsions is 615 μ , distributed over a very narrow interval. The corresponding kinetic energy is 4.8 MeV. If the pion decays at higher energies (before it slows down) the muons have a range greater than 615 μ . On the other hand, if the pion escapes this decay, then as it slows down to about 10 MeV, its rate of ionization increases slowly to several times minimum ionization, resulting in the typical Bragg curve. Whether or not a pion survives the decay process depends to a great extent on the comparison of the distance that the meson traverse before decaying with the actual experimental

distances involved. For this experiment the fraction of pions lost in the decay process was very small. (≈ 10 to 15%).

In addition to electronic inelastic collision events, the surviving mesons also encounter nuclear events in their travel. The possible modes of nuclear interaction may be broken down into the processes of scattering (both elastic and inelastic) by nuclei and absorption by nuclei. The significance of scattering (particularly inelastic scattering), with its concomitant loss of particles from the beam, has already been related. Studies on the nuclear interaction of 30- to 110-MeV π^- in thick emulsions have been performed by Bernardini.⁵⁵ As far as the elastic and inelastic scattering events are concerned, the π^+ behaves roughly in the same way as the π^- . This study indicates an elastic scattering cross section (for elastic scatterings greater than 30°), for pion energies of 30 to 50 MeV, of 0.19 barn, as compared with an inelastic cross section of 0.06 b for the same energy range. In the energy range 100 to 110 MeV, the elastic cross section is 0.16 b, compared with 0.25 b for the inelastic collision cross section. It is readily apparent from these data that the cross section for inelastic scatterings increases rather markedly with increasing energy, while the elastic cross section decreases somewhat. Additionally, the average energy loss in these inelastic scattering events was observed to be very large, more than 50% of the incident energy. Bernardini's results also indicate a total interaction cross section for π mesons with the nuclei of the emulsion close to the geometrical cross section. The end result of these inelastic (both nuclear and electronic) and elastic nuclear collisions is to effectively thermalize the pions.

The π^+ thus slowed down to thermal energies experiences a repulsive force from the atomic nuclei. Therefore, it can never approach a nucleus closely enough for an interaction to occur, and it eventually disappears by spontaneous decay. A study in photographic

plates reveals that virtually all the observable positive mesons disintegrate into positive muons of mean energy 4.18 MeV after coming to rest in the emulsion. These muons then travel about 615 μ in emulsion and subsequently decay according to the equation

$$\mu^{\pm} \rightarrow e^{\pm} + \nu + \bar{\nu} .$$

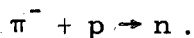
The mean life for this decay process at rest is 2.15×10^{-6} sec. In contrast to the muons resulting from pion decay, the electrons from μ -meson decay do not have a unique energy. There is a continuous distribution, with a maximum energy of the decay electrons of 55 MeV and a measured average energy of 34 MeV.⁵⁶

Despite the tremendous differences in the rates of nuclear absorption of slow π^{-} and μ^{-} mesons and the qualitatively different nuclear effects observed when absorption takes place, the slowing down and capture of slow π^{-} and μ^{-} mesons is essentially the same process for both. This is because the slowing-down and capture process depends largely upon the charge and mass of the meson, and the charges are the same and the masses differ by only 30%. Slow negative mesons (both π^{-} and μ^{-}) are promptly captured by the electric attraction into a Bohr orbit in the neighborhood of a nucleus to form a mesic atom. If μ^{-} mesons, are present in the beam, they behave quite differently from π^{-} mesons when absorbed by atomic nuclei, in that no stars are formed. Although slow μ^{-} may be trapped quite rapidly in appropriate orbits to form μ -mesonic atoms, the probability of nuclear absorption is much less than with the corresponding π -mesonic atoms. The important consideration is the relatively weak interaction between muons and atomic nuclei. For nuclei with atomic number less than approximately 12, negative muons generally survive absorption, and decay (like the positive muons) into a negative electron and two neutrinos. In this region the lifetime for nuclear absorption is approximately equal to the lifetime for

electron decay of the negative muon. With nuclei of increasing atomic number, the probability of absorbing the negative muon increases. The final result of the absorption is believed to be



π^- Mesons appear always to undergo nuclear capture, never spontaneous decay, after coming to rest in photographic emulsions. Since these emulsions contain light as well as heavy elements, π^- mesons are more likely to undergo nuclear absorption than spontaneous decay in all substances, whereas for μ^- mesons this is true only in substances of higher atomic number. Like the μ^- , the π^- is captured into a stationary Bohr orbit to form a mesic atom. The radius of a Bohr orbit of the mesic atom is much smaller than the radius of a Bohr orbit of the ordinary atom, approximately in the inverse ratio of the masses. In fact, for very heavy elements, the first Bohr orbit of the mesic atom is comparable to the nuclear radius. At first, the negative meson is trapped in one of the outer mesonic energy levels. As a result of the electrostatic attraction by the nucleus, it then makes a transition to the next inner level and then to the next and so on. Every transition is accompanied by the emission of characteristic mesonic x rays. The π^- meson is subsequently absorbed by the nucleus and combines with one of the protons in the nucleus, changing the proton into a neutron according to

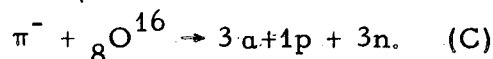
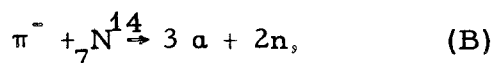
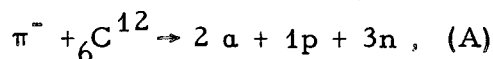


Since the rest energies of the proton and neutron are nearly equal, this equation represents a release of energy practically equal to the rest energy of the π^- meson, which is followed by the "evaporation" (or "explosion") of the residual highly excited nucleus. The neutron resulting directly from the absorption of the meson does not acquire all the energy released by the disappearance of the meson, but usually collides with other nucleons, distributing most of its energy

among them and thus giving rise to the nuclear explosion fragments. Investigations with photographic emulsions reveal that about 27% of the negative mesons fail to produce visible stars at the ends of their tracks.⁵⁷ It is likely that in these cases the energy released by the disappearance of the π^- meson is carried away by neutrons, and perhaps to a great extent by the neutron resulting directly from the pion interaction. The remaining 73% of the negative π mesons give rise to visible stars at the ends of their tracks in the emulsion. These stars usually have one, two, or three prongs representing α particles and protons. Menon et al. performed an investigation of these stars in emulsion, separating the disintegrations of heavy nuclei (Br, Ag) from light nuclei (C, N, O).⁵⁸ An observation of the total star population represented in each component of the emulsion revealed that 46% of the stars due to capture of π mesons corresponded to the lighter nucleus component and 54% to heavy nuclei. The distribution of these stars according to number of prongs, for stars originating in light and heavy nuclei separately, indicated that for heavy nuclei the prong distribution was heavily weighted toward one- or two-pronged stars, in contrast to the relatively even distribution of one-, two-, and three-pronged stars (with an actual preponderance of three-pronged stars) for the light nuclei. The energy spectra of these nuclear fragments in the different component nuclei also appear to be different. The energy spectrum of protons of less than 30 MeV shows a peak at 9.6 MeV. On the other hand, the α -particle spectrum is seen to have a double peak with a transition point at about 9 MeV. Probably, most of the α particles below 9 MeV originate from the light nuclei (C, N, O) in the emulsion and those above 9 MeV from the heavy nuclei (Ag, Br), because of the difference in Coulomb barriers. For decreasing Z, the Coulomb barrier is relatively smaller for α particles and therefore one would expect a larger ratio of α particles to protons for the lighter nuclei. Indeed, it has been shown that for light nuclei the ratio is approximately unity, while for heavy nuclei the ratio decreases to 0.3.

In addition to protons of less than 30 MeV (mainly evaporation protons) associated with π^- stars, Menon,⁵⁸ in agreement with Cheston and Goldfarb,⁵⁹ showed that about 10% of the π^- mesons ending in the emulsion give rise to protons with energies considerably greater than 30 MeV.

From the point of view of its nuclear composition, biological tissue can be regarded as made up of hydrogen, carbon, nitrogen, and oxygen. The nuclear disintegrations which are of greatest importance for our purposes then involve the light-nucleus tissue constituents--carbon, nitrogen, and oxygen. In hydrogen, the π^- mesic atom resulting from capture migrates a short distance in the tissue until it encounters a heavier nucleus to which the π^- meson is transferred. The reactions of the light nuclei may be classified, according to those most frequently observed, as follows:



Menon has measured the frequency of occurrence of the three above reactions in a study of stars produced in gelatin (sandwiched in between layers of emulsion). Fifteen percent of the stars represented one of the three reactions; more precisely, 7.6%, 3.7%, and 4.2% represent reactions (A), (B), and (C), respectively. According to Fowler and Perkins, Eq. (A) appeared to be the most common reaction, accounting for about 25% of the cases.²⁹ The α -particle spectra as reported by Menon for C and O extends to about 25 MeV, while for N the cutoff is at about 15 MeV.

Ammiraju performed a later study of the disintegrations in light nuclei under conditions in which the complications due to the presence of heavy nuclei are eliminated.⁶⁰ This work investigated the absorption of slow π^- in carbon and nitrogen.

There is very good agreement of Ammiraju's study with Menon's alpha spectrum in nitrogen; both show an alpha spectrum extending to about 15 MeV, with a preponderance of alpha particles with energy less than 10 MeV. Such low-energy alpha particles have been explained by the deuteron absorption model in which most of the rest energy of the pion is given to the loosely bound deuteron in N^{14} , and the residual C^{12} fragment subsequently decays into three low-energy alpha particles.⁵¹ The results for carbon are likewise in generally good agreement with Menon.

IV. RESULTS AND DISCUSSION

The results reported here were taken from several different experimental π^- meson beams. Although this certainly does not preclude a meaningful correlation between the data taken from different beams, we must at the same time admit that the analysis has not been made any easier by this difference. The various beams to be discussed are described in Table II.

Some preliminary measurements were made in the meson cave, immediately downstream from the bending magnet, using industrial x-ray film sandwiched between 1-inch slabs of Lucite and positioned along the horizontal beam plane. The results indicated that the general radiation background in the cave was much too high to permit useful data. Consequently, all subsequent runs were performed behind a 4-foot-thick concrete shielding wall placed in the cave.

First, intensity measurements were made with an A-CO₂-filled monitor chamber placed in the pion beam. The beam intensity is generally measured in an ionization chamber which has been calibrated against a Faraday cup at different energies. However, in this experiment, the intensity is much too low to permit useful measurements with a Faraday cup. Therefore it was necessary to calculate the ion-chamber calibration-factor constant appropriate for the beam energy used according to the expression

$$F = \frac{t}{w} \left(- \frac{1}{\rho} \frac{dE}{dx} \right), \quad (21)$$

where t is the thickness of the chamber in g/cm^2 of argon, w is the energy loss per ion pair formed, and $-\frac{1}{\rho} \frac{dE}{dx}$ is the mass stopping power in argon at that energy.

The energy loss per ion pair formed, w , is equal to 26.4 eV for argon, and it is independent of the energy of the primary particle. The calculated value of the most probable energy loss for 90-MeV

Table II. Experimental beams.

Run number	Bending magnet	Doublet quadrupole	Target radius (in.)	Target azimuth (deg)	Pion energy (MeV)
1	Orion	Hero	82.2	251	90
2	Orion	Hero	82.0	250	90
3	Achilles	Hero	83.0	251	101

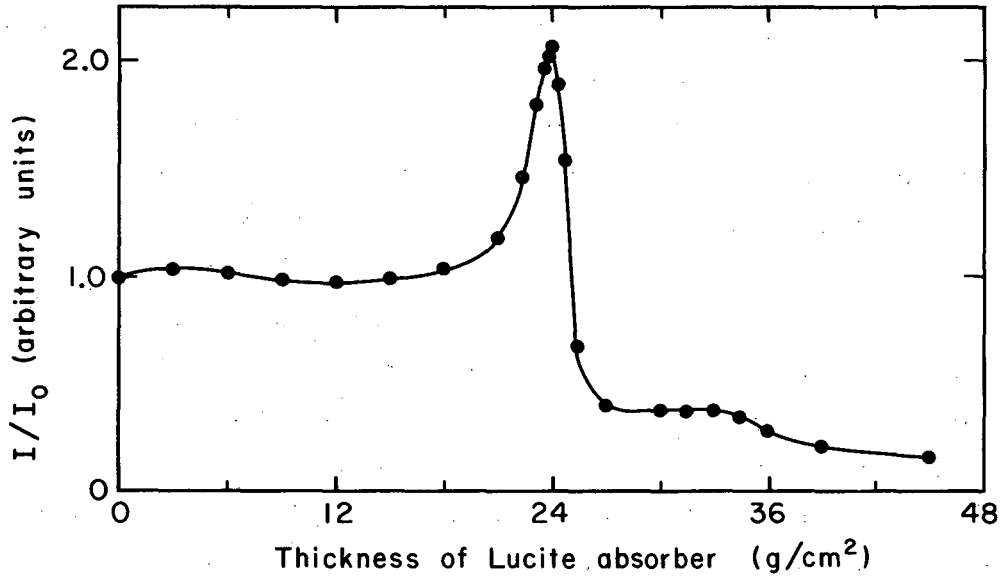
pions in argon is 1.16 MeV/g/cm^2 . The thickness of the chamber in the direction of the beam is $9.55 \times 10^{-3} \text{ g/cm}^2$. Substituting these values into Eq. 21, one obtains a constant value for the chamber of 1.49×10^{16} particles per Coulomb. That is, every Coulomb of charge collected by the ion chamber represents the passage of 1.49×10^{16} particles through the chamber.

The beam at entry in runs #1 and #2 had a circular cross section of 45.5 cm^2 ; this was confirmed by exposing x-ray film positioned normal to the beam. The momentum spread of the beam was 5%.

If we neglect for the moment the beam contamination by electrons and muons, the pion flux can be readily obtained by simply applying the calibration factor to the uncorrected integrated current. The integrated current in the ionization chamber was measured by passing it into a condenser and measuring the potential across the condenser with an electrometer circuit. The total capacity in the integration circuit is $0.01 \mu\text{F}$. The integrator circuit reads full scale with 10 mV at the input. This method yields a pion flux (including background) of $7.83 \times 10^2 \pi^-/\text{cm}^2 \text{ sec}$. Although this value is obviously quite low, it is no cause for concern at this point, since this is by no means the maximum attainable flux.

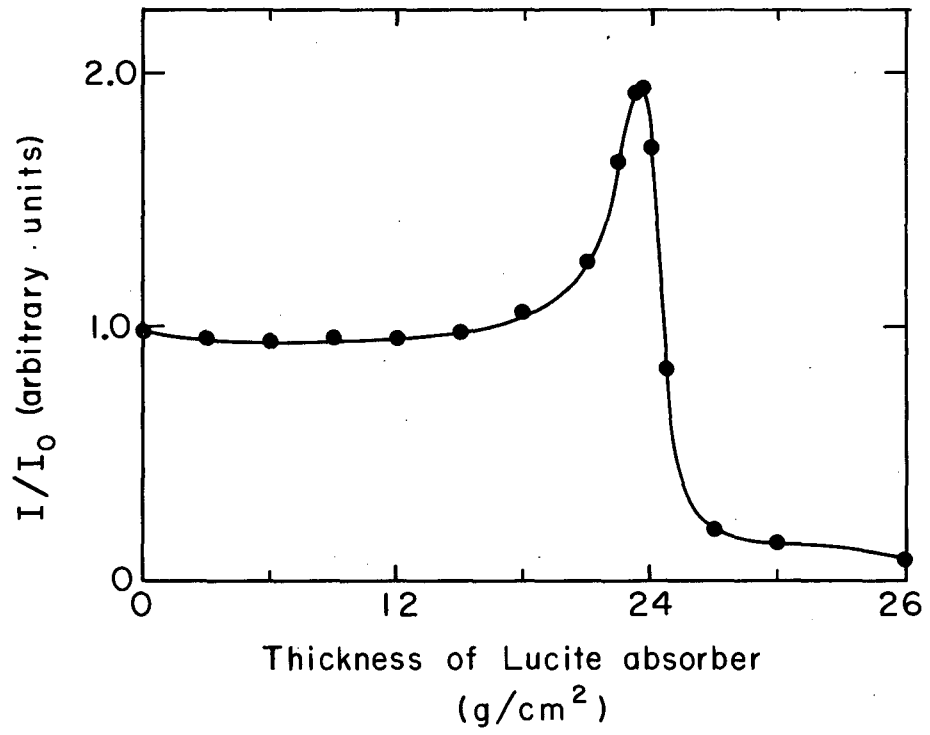
A Bragg curve was then obtained as discussed on page 64, with a second ionization chamber identical to the monitor chamber, and with different thicknesses of Lucite absorber interposed between the two. Measurements were made for both π^- and π^+ beams. In this way one would hope to observe the alteration of the typical Bragg curve resulting from the capture phenomenon at the end of the π^- -meson range. The Bragg peak for π^- mesons should be greater than and of different shape from that for π^+ mesons. The difference between the two peaks is a measure of the average energy release from capture events in a beam of π^- .

Figures 23 and 24 show the results of these experiments, where the measurements of the pion beam in the detector chambers (I) have both been normalized to the monitor chamber (I_0). It is quite apparent



MU-34191

Fig. 23. π^- -Meson Bragg curve.



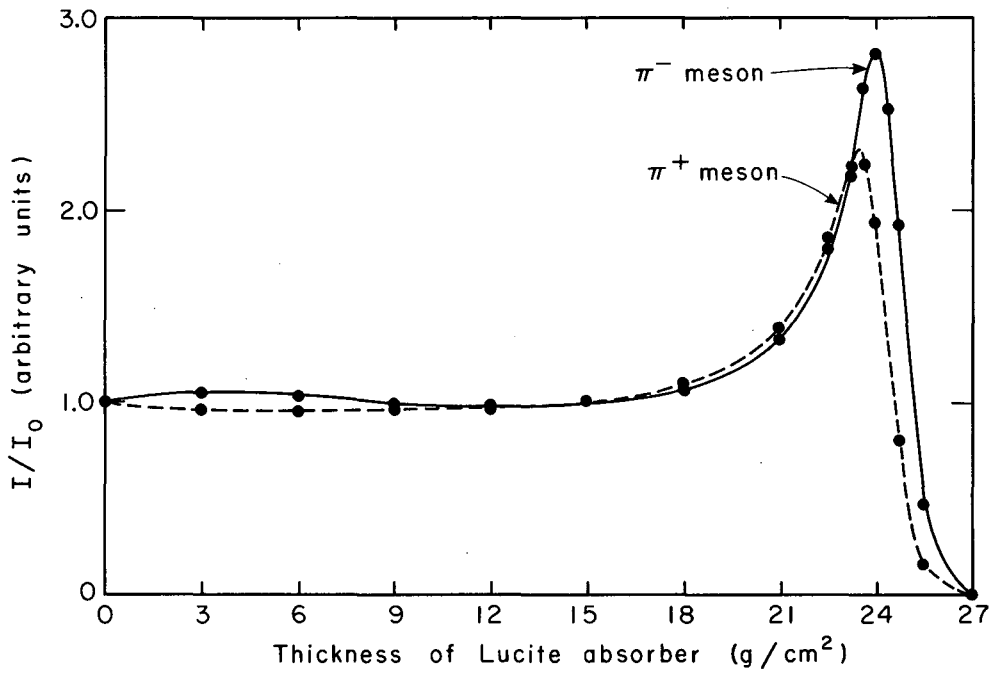
MU-34192

Fig. 24. π^+ -Meson Bragg curve.

that there is no sizable difference between the two curves. However, for the comparison to be more meaningful we must first subtract the background from each of the curves. Because of the uncertainty involved in the assessment of the electron contamination from the information available thus far, any correction for the background should be viewed as strictly approximate. A very rough approximation to this background may be made by assuming those relatively broad muon and electron plateau regions of the curve persisting beyond the Bragg peak as representing the total muon and electron contamination at all points along the curve.

A total contamination ($\mu^- + e^-$) of about 40% is obtained by using this method. The incident beam intensity corrected for background is then $4.7 \times 10^2 \pi / \text{cm}^2 \text{ sec}$. A comparison, with the background subtracted and the results normalized to unity (relative to zero absorber thickness), is shown in Fig. 25. There is a difference both in shape and in height of the two curves, with the peak intensity for π^- mesons exhibiting an increase of about 22% above that for the π^+ Bragg peak. Furthermore, the π^- peak has been shifted to the right of the typical Bragg peak as represented by the π^+ mesons. The new position of the peak corresponds roughly to the probable range of 90-MeV pions. This range is approximately 1% greater than the published mean range for 90-MeV pions. At any rate, this region also represents the area where most of the pions are stopping, and it should therefore exhibit the greatest pion-capture activity.

However, the π^- meson peak is not augmented as much as one might expect it to be, which is due mainly to two factors; (a) the nuclear fragments produced by the capture of the π^- mesons have ranges much larger than the size of the chamber; (b) the number of pions that actually stop in the chamber and are captured is quite small. For example, the range of the protons resulting from star events is more than 20 times the thickness of the chamber, while that for the α particles is roughly equal to the chamber thickness. That is, for stars that are produced immediately adjacent to the front wall of the chamber,



MU-34193

Fig. 25. Comparison of Bragg curves for π^- and π^+ mesons.

roughly 1/20 of the proton energy is absorbed while all the α energy is deposited. However, most of the stars are not formed in this region, but are distributed over the entire chamber, thus depositing a considerably smaller amount of their energy in the chamber. As a result of this "wall effect" the stars that are formed contribute to the production of ionization in the chamber only a small fraction of the energy released. In addition, the difference between these curves might also be affected to some extent by a contribution to the π^+ -meson peak by positrons arising from the decay of μ^+ mesons in the chamber.

The distribution of total ionization along the path of a particle is, in first approximation, the same as that of the rate of energy loss. That is in gases, $-\frac{1}{\rho} \frac{dE}{dx}$ can be found from the specific ionization, if the factor w is known for the particle and for the energy and type of gas concerned. The quantity thus obtained is usually the average energy loss, with the individual energy losses represented by the familiar symmetrical (or Gaussian) distribution about the average value. Because of the low stopping power of the chamber used in this experiment large fluctuations in the energy loss and resultant ionization are expected, which may be represented by the asymmetrical distribution curve calculated by Landau.⁴⁹ This behavior, involving very small energy losses, is in contrast with the symmetrical distribution in which larger losses, up to a maximum, Q_{\max} , are experienced. In fact, at 90 MeV the maximum energy, Q_{\max} , that a pion may lose in a collision with an orbital electron is 1.7 MeV, while the individual energy loss, W_1 that occurs just once in traversing the small effective chamber thickness over which the energy loss is being observed is about 1 keV. It then follows from the discussion on page 62 that the quantity measured in this experiment is the peak of the asymmetrical distribution that corresponds to the most probable energy loss. As the energy of the pion decreases, the difference between W_1 and Q_{\max} also decreases until, at about 2 MeV, $W_1 \approx Q_{\max}$, and the average energy loss then equals the most probable energy loss in the chamber. Table III shows a comparison of the calculated probable energy loss and the average energy loss for

Table III. Comparison of calculated values for most probable energy loss and average energy loss.

E_{π} (MeV)	Q_{\max} (MeV)	W_1 (MeV)	$-\frac{1}{\rho} \frac{dE}{dx}$ _{av} (MeV/g/cm ²)	$-\frac{1}{\rho} \frac{dE}{dx}$ _{prob} (MeV/g/cm ²)
100	2	1×10^{-3}	1.55	1.095
90	1.72	1.06×10^{-3}	1.66	1.16
80	1.52	1.11×10^{-3}	1.73	1.20
70	1.29	1.19×10^{-3}	1.82	1.27
60	1.07	1.29×10^{-3}	1.94	1.38
50	0.87	1.44×10^{-3}	2.11	1.54
40	0.67	1.67×10^{-3}	2.40	1.78
30	0.49	2.04×10^{-3}	2.88	2.16
20	0.31	2.81×10^{-3}	3.80	2.96
10	0.15	5.11×10^{-3}	6.20	5.38
5	0.08	9.16×10^{-3}	11.3	9.66
2	0.03	2×10^{-2}	21.2	21.1

π^- mesons. The values for the average energy loss were taken from the range-energy curves for protons given by Aron.⁶¹ Since, for incident particles of identical charge moving in like absorbers, $-\frac{1}{\rho} \frac{dE}{dx}$ is a function of the velocity only, then if $-\frac{1}{\rho} \frac{dE}{dx}$ as a function of energy is known for protons it can be found for pions by simply changing the energy scale so that the new energy values are smaller by the ratio $M_{\text{pion}}/M_{\text{proton}}$. According to these calculations the experimental values for energy loss in the chamber should be 30% less than the values suggested by the average energy loss tables.

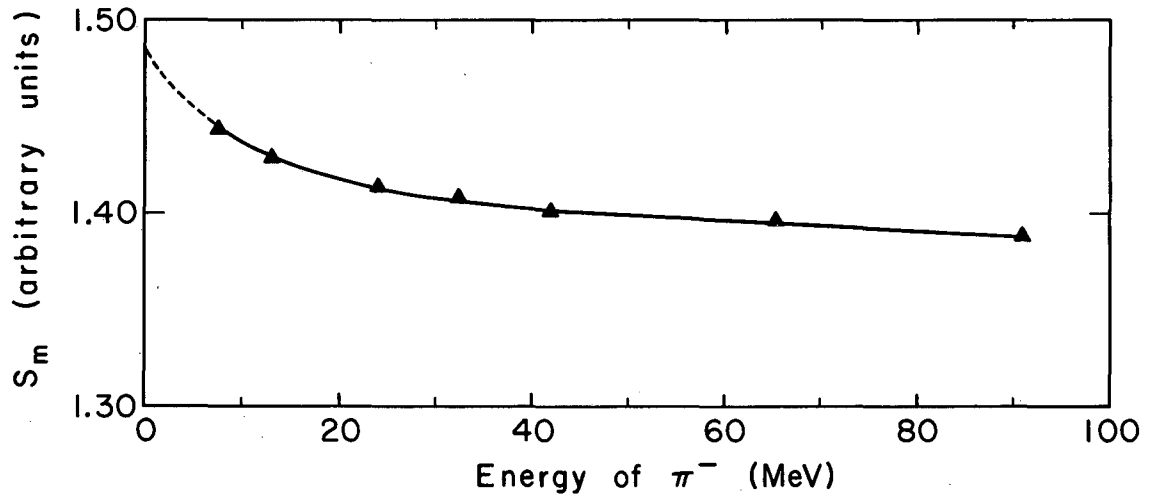
Ideally, the validity of the experimental results is checked by comparing them with the theoretical calculations of energy loss (in this case, the probable energy loss). This would mean that the ion chamber data must be expressed in terms of the probable specific ionization per pion, from which we may then calculate the probable energy loss per pion. In order to express the experimental results in terms of the energy loss per pion we must first determine the number of pions as a function of distance. Although the ion chamber was used to obtain an approximate value for the beam intensity, there are several reasons why the chamber data are unsatisfactory for an accurate measurement of pion number: (a) the beam intensity measurements include an electron-plus-pion background that cannot be precisely determined from ion chamber data alone, (b) the equation for the calibration factor used in the calculation of beam intensity contains the stopping power for a single particle and does not account for changes in stopping power that result from straggling, (c) the single-particle stopping power may be modified to some extent by the presence of the electrons. One solution is to use the integral range method for obtaining this information. Unfortunately, integral range measurements were not made in this run, so that the pion number was not available and it was not possible to make a comparison in terms of energy loss per pion.

If we consider the intensity distribution of the pion beam to be relatively homogeneous over the beam cross section, the dose at the

position of the ionization chamber is given as

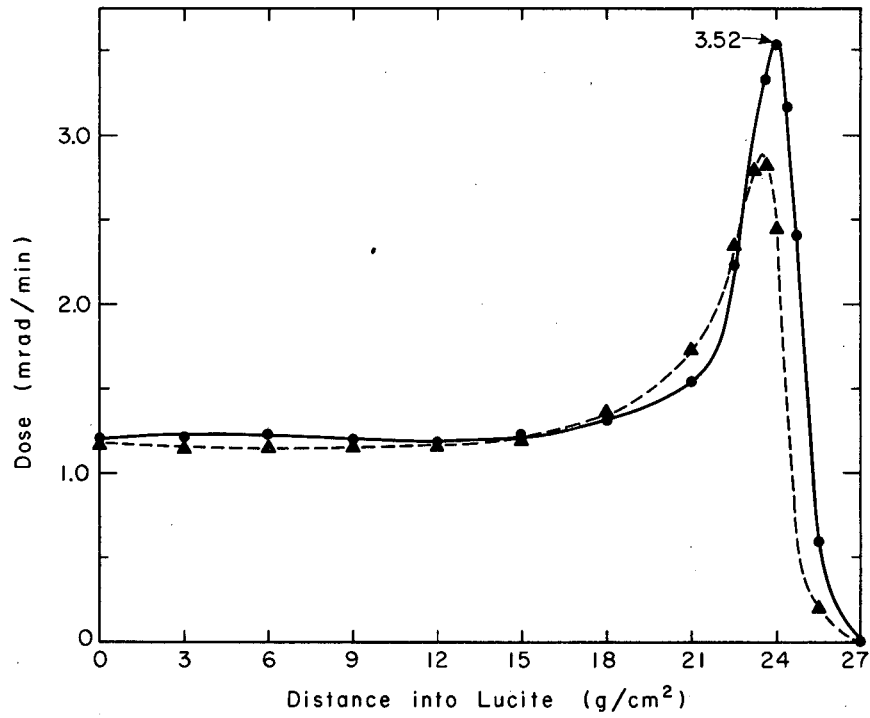
$$D = \frac{Q w S_m \times 10^5}{V \rho} \quad (22)$$

where ρ is the density of argon in the chamber at the particular temperature and pressure, D is the dose in rad/min, Q is the charge in Coulombs per minute collected in the chamber, V is the collection volume in cm^3 , w is the energy in eV per ion pair for the argon in the chamber, and S_m is the mass-stopping power of Lucite relative to that of argon. The collection volume of the chamber was assumed to be defined by the cross-sectional area of the beam and the depth of the chamber. The results for the calculation of S_m are shown in Fig. 26. Since S_m is a function of the energy of the pion, a determination must be made of the average energy of the pions corresponding to the different measurement depths, by use of range-energy curves for Lucite. Strictly speaking we will then have the absorbed dose in Lucite, which is very close to that in tissue. The calculated doses are shown in Fig. 27. Because of the complexity of the problem, several approximations are involved in these calculations, such as (a) at low pion energies it is extremely difficult to determine an average energy; (b) in the low-energy regions there are no accurate values of S_m , and simple extrapolation to zero energy with $\lim_{E \rightarrow 0} S_m = 1.485$ was used quite arbitrarily; (c) the background correction is a rough approximation; (d) the assumption that the intensity distribution of the pions is homogeneous over the beam cross section may not be correct. According to these results the maximum attainable π^- -meson dose is about 3.5 mrad/min (at the peak). The tumor-skin dose ratio is 2.96, with a full width at half maximum (FWHM) for the Bragg peak of 1 inch. In contrast, for protons, Larsson reports a tumor-skin dose ratio of 2.3 for full width at half maximum value of 1 inch in water.⁶² This slightly larger tumor-skin dose ratio with pions (for equal FWHM values of proton and pion) is particularly



MU-34194

Fig. 26. Relative mass stopping power of π^- in Lucite compared with argon.

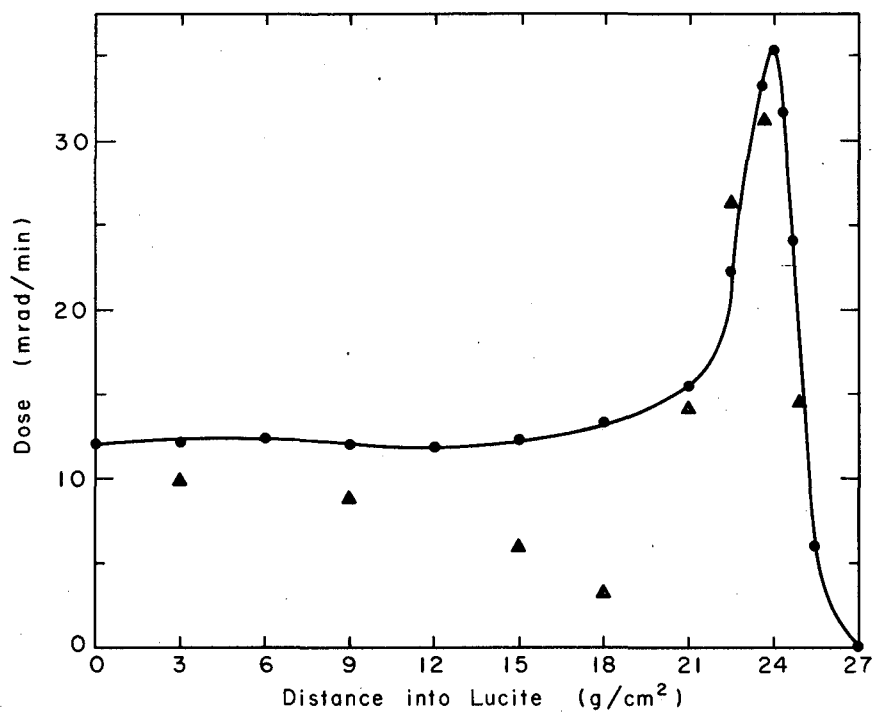


MU-34195

Fig. 27. Absorbed dose calculated from ionization chamber measurements.
● π^- meson
▲ π^+ meson

important when one is attempting to distribute the particle energy so as to give uniform irradiation of large volumes located within the Bragg peak. Furthermore, it is possible that this dose ratio for pions may actually be further increased by using a lower incident pion energy; the observed ratio may also be increased by more effective detection of the nuclear fragment energy. Nevertheless, the chamber has recorded an increased peak dose, presumably from the star fragments, of the order of from 20 to 25%. This difference should be further augmented by the increased linear energy transfer in the star region and its concomitant increase in biological effectiveness. At present it does not seem unreasonable to expect an average LET in the star region of about 40 to 50 keV/ μ , with an RBE of about 3 or 4, depending upon the biological system used. Although the above predictions are more than simple conjecture, they must still depend upon future investigations for their experimental verification.

The absorbed dose recorded by the ion chambers may then be compared with the results from the lithium fluoride dosimeters shown in Fig. 28. Although no work with these dosimeters for pions has yet been reported, preliminary investigations using protons, α particles, and heavy ions indicate that pions should not be much different from any other charged particle.⁶³ A comparison of the curves reveals that these two systems differ by a factor of about 10 in recorded dose. This difference may be partly accounted for in two ways: (a) the LiF dosimeters may respond to the ambient neutron and γ -ray background, whereas the chamber is relatively insensitive to these radiations (b) although we have assumed a uniform intensity distribution over the beam cross section, it may not be uniform. If the intensity were much higher along the central axis of the beam (which is where the dosimeters were located) the measured dose would be proportionately higher. Except for the constantly decreasing initial portion of the LiF curve compared with the relatively broad flat initial response of the ion chamber, the shapes of the two curves are not very different. The difference in



MU-34196

Fig. 28. LiF dose determination for π^- -meson beam.
● ion chamber $\times 10^{-1}$
▲ LiF dosimeter $\times 10^0$

the two curves is because of the small size of the LiF dosimeter in comparison with the beam cross section, so that the dosimeter is sensitive to the loss of pions from the beam by inelastic scattering events; the ion chamber, on the other hand, presents a cross section that is quite a bit larger than the beam and is therefore not so sensitive to this loss. The LiF results roughly confirm the shape of the Bragg peak observed with the chamber. The full width at half maximum is about 1 inch for a 5% spread in momentum. The tumor skin-dose ratio for both systems is almost 3 to 1. Like the ion chamber, the LiF dosimeters have a basic limitation at the Bragg region, for they show a reduction in sensitivity by as much as 70% for high-LET radiations (50 keV/ μ). Consequently, the ratio of tumor dose to skin dose is probably must higher than is indicated here.

A silicon surface-barrier-type solid-state detector was used in an attempt to obtain a more definitive appraisal of the contribution of the nuclear fragments to the tumor-skin dose ratio. Because of its relatively high stopping power this device should be quite effective in detecting the star events. In particular, the depletion layer was chosen to correspond to the range of the nuclear fragment of greatest importance to us--the α particle. The depletion layer had a thickness of 4.54×10^{-2} g/cm², which was more than sufficient to completely absorb the energy of the 6-MeV-average α -particle fragments. This thickness of silicon roughly corresponds to the ranges of a 22-MeV α particle, a 5.2-MeV proton, and a 0.22-MeV electron. Hence a sizable portion of nuclear energy released by way of the proton escapes from the detector. Likewise, the contribution to detector response by the incident pions, muons, and electrons is very small.

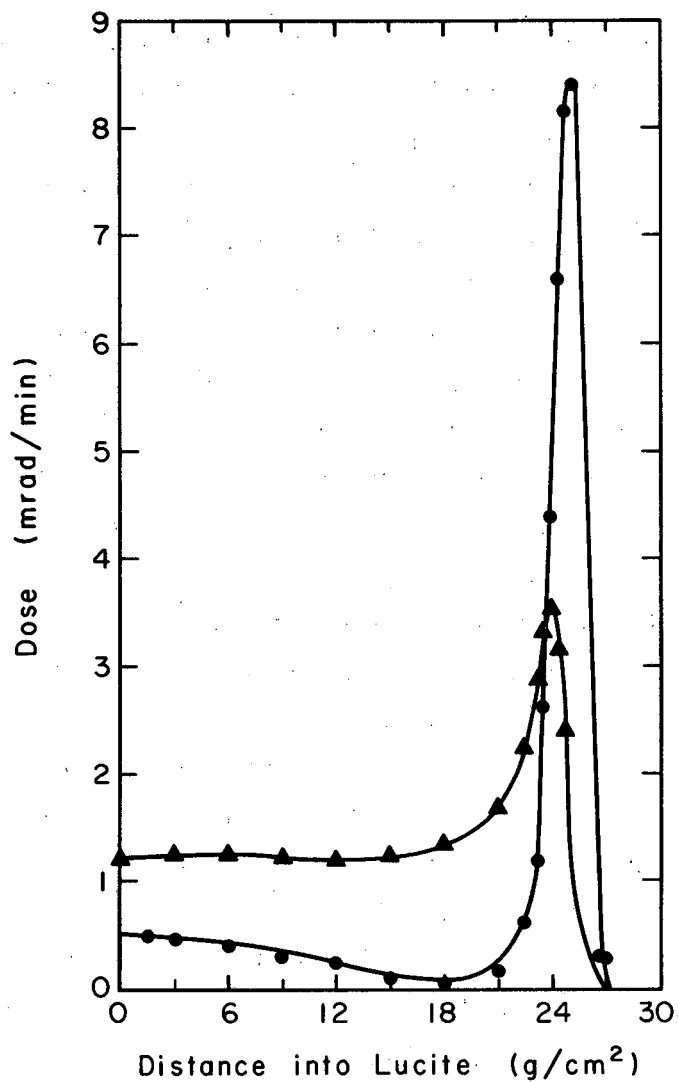
For any thickness of Lucite absorber, the product of energy per channel and the total counts in that channel integrated over all the channels gives the total energy deposited in the depletion layer of the detector. The system was calibrated with the 5.49-MeV α particles from an americium-241 source. The peak of the energy distribution resulting from these alpha particles was positioned to correspond to

channel number 68 in a 400-channel analyzer. Since the detector responds linearly, a single count in a particular channel then corresponds to an energy deposition of 80.5 keV times the number of that channel. The total energy deposited in the depletion layer, expressed in MeV/g, may then be readily converted to absorbed dose in Lucite.

The results are shown in Fig. 29. Once again because of the smallness of the silicon detector (4 mm^2), we have a definite slope in the initial portion of the curve the same as we observed for the LiF dosimeters. The Bragg peak obtained with the detector shows a full width at half maximum (FWHM) of about 0.8 inch, which is not too different from the 1-inch FWHM for the ion chamber and LiF results. However, the peak dose of 84 mrad/min for the silicon detector requires some further explanation before it can be meaningfully compared to the ion chamber data. Because of the small size and the position of the detector along the central axis of the beam, it is reasonable to expect it to behave in the same way as the LiF detector. That is, if there is a sizable inhomogeneity of the beam cross section (and later experiments will show that such is the case), then the highest intensity will most likely be along the central axis of the beam.

Therefore, a detector with a small cross section compared with the beam (i. e., the solid-state or LiF detector), centered on this axis, gives a higher dose than a detector whose cross section is larger than the beam. Indeed, a good part of the difference in Fig. 29 between the doses measured by the silicon detector and by the ion chamber may be explained in this way.

Despite this difference in absolute doses, the relative values of the dose of the peak compared with the entrance dose (i. e., tumor-skin ratio) should be relatively constant. The measurement of this ratio with the solid-state detector yielded a value of approximately 17, which is greater than the tumor-skin ratio measured with the ion chamber by a factor of almost 6. Since the detector response has been maximized for response to the alpha fragments, one is tempted to assume that this sizable increase in energy deposition is due mainly



MU-34197

Fig. 29. Depth dose for 90-MeV π^- mesons in Lucite.
● surface-barrier detector $\times 10^1$
▲ ion chamber $\times 10^0$

to the α particles from the star events. A check on this assumption was made by calculating the amount of energy that must be absorbed by the detector for each pion that, on the basis of solid-state results, is stopped. According to these calculations, for each pion stopped in the detector there is an energy absorption of 16.4 MeV. Fowler and Perkins estimate that for each pion stopped in tissue (and subsequently captured by the tissue nuclei) there is a release of approximately 30 MeV from the ensuing star event in the form of α particles and protons.²⁹ Our results compare quite favorably with this work when one considers that most of the proton energy escapes from the detector and that the stars formed in silicon may be quite different from those formed in tissue. Run #3 was designed to yield a more definitive appraisal of the pion beam and to extend the use of ion chambers to include those filled with nitrogen under both high and low pressures.

The low-pressure argon-filled chamber again served as a monitor of the beam, just as it did in runs #1 and #2. First, an integral range curve was obtained by the method described on page 24. An average pion energy of 101 MeV (196 MeV/c in momentum units) was determined by taking the average of the energies corresponding to the pion ranges at points A and B (94.5 MeV and 108 MeV, respectively) of Fig. 7, found from range tables.³⁶ The spread in the pion energy is half the difference between these two energies, or ± 6.75 MeV. This spread in pion energy corresponds to a spread in momentum of ± 8.4 MeV/c, which in turn may be expressed as a total momentum spread of 8.6% (± 4.3). The muons resulting from the decay of pions before the beam reaches the analyzing magnet have the same range of momentum as the pions. Because of their mass difference, pions and muons of the same momenta have different energies. In this case, these momenta correspond to a range of muon energies which extends from 100 MeV to 123 MeV, with an average energy of 116 MeV. Because of this difference in energy, muons exhibit a range which is on the order of 30% greater than pions of the same momentum. Consequently, if the muon contamination represents a sizable

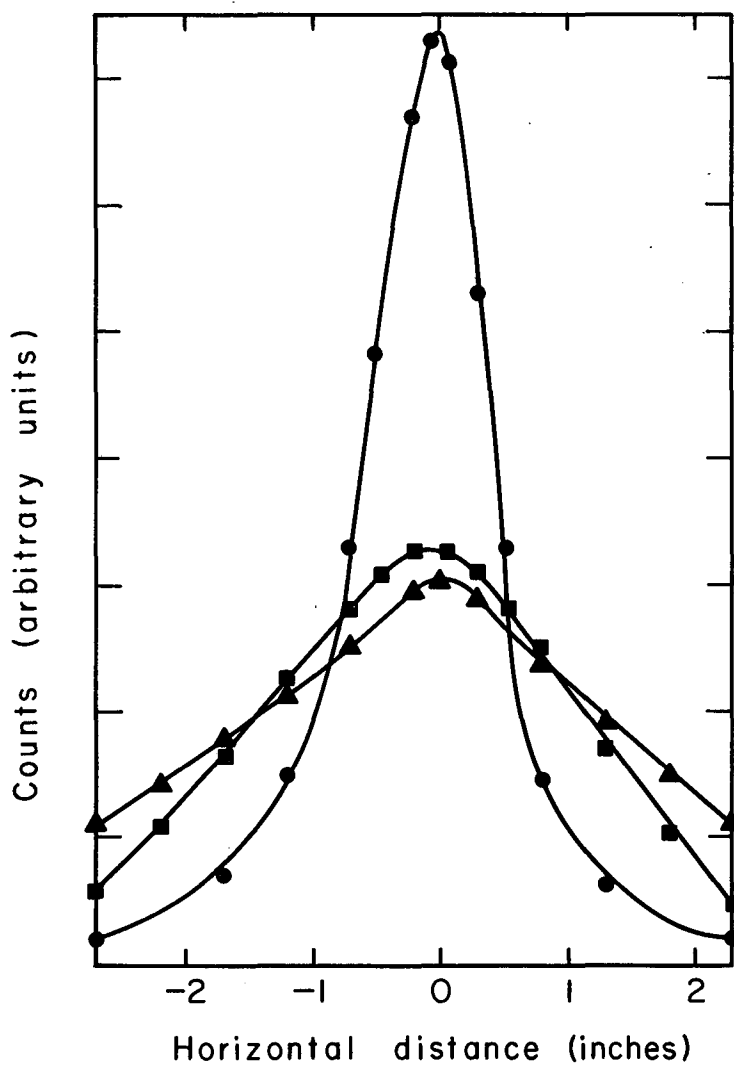
fraction of the total beam, it may seriously affect the localization of energy. For this pion beam the muon contamination was 12%.

An estimation of the electron contamination may be obtained by a linear extrapolation of point B' to zero absorber thickness. This method gives a result which is generally within 30% accuracy.⁶⁴ An electron contamination of 24% was observed. Since the integral range curve is essentially a number-distance curve, it is an important source of information regarding loss of pions from the beam as a function of absorber thickness. From zero absorber thickness to break A in Fig. 7 represents the total losses from the beam before the end of the range, which in this case amounts to 40% of the original particles. According to the integral range data, the maximum intensity for this particular pion beam, after corrections for the muon and electron contaminations are made, is $1.56 \times 10^4 \pi^- / \text{cm}^2 \text{ sec}$. A measurement of the maximum intensity, using the monitor chamber and correcting for beam contamination, gave a value of $2 \times 10^4 \pi^- / \text{cm}^2 \text{ sec}$. This is a factor of about 40 greater than the intensities obtained in runs #1 and #2.

The beam profile results are quite useful in more rigorously defining the structure of the beam cross section, as shown in Figs. 4 and 5. The full width at half maximum of the beam is 1.125 inches and 3.25 inches for the horizontal and vertical profiles, respectively. The horizontal profile is down to 10% of its peak value at a FWHM value of 3.06 inches, while the vertical profile expands to 6.5 inches ((is doubled) for the same reduction in intensity. This appraisal enables one to more judiciously select an effective beam cross section to be used in the calculation of dose from ion chamber data. Even after this correction is made, the calculations represent only an average dose over the whole chamber, as discussed earlier. This macroscopic measurement of the dose would not be accurate for estimating the dose delivered to biological systems, which are much smaller than the chamber.

Two different thicknesses of Lucite absorber were then interposed between the incident beam and the detectors in order to obtain a qualitative assessment of the extent of beam divergence as a function of absorber thickness. The results are shown in Fig. 30. There is a definite increase in uniformity of the beam cross section with increasing absorber thickness, accompanied by a decrease in peak intensity. The lateral spreading (or smearing) of the beam, which causes the increased uniformity of the beam intensity, is mainly due to Coulomb scattering, whereas the sharp decrease in the peak intensity is probably due to both Coulomb and inelastic nuclear scattering. An absorber thickness of 7.5 inches of Lucite introduced a lateral spread of the beam by about 1.25 inches, while the peak intensity appears to have been reduced by a factor of about 2.5.

A second attempt was then made with ion chambers in hopes of confirming the particularly encouraging results obtained with the solid-state detector. We have already noted that the low-pressure chambers had an effective chamber thickness which was but a small fraction of the total range of the nuclear fragments resulting from star events. Consequently, the augmentation of the Bragg peak by these fragments (mainly α particles) was very small, and most of their energy was deposited outside the chamber. It was then reasoned that, since the energy loss is proportional to the electron density, we should simply increase the density (by increasing the gas pressure) in the chamber, thereby increasing the effective chamber thickness and absorbing more of the nuclear fragment energy. Ideally, one would like to have a gas-filling pressure that approaches unit density (although it is not practical). The chamber results reported here are for a nitrogen gas pressure of 205 psi (approx. 14 atmospheres above atmospheric pressure), which is still almost two orders of magnitude less than unit density. The range of the nuclear fragments, expressed in g/cm^2 , is approximately 25% less in nitrogen than in argon. This behavior is due to the difference in their respective electron densities and average



MU-34198

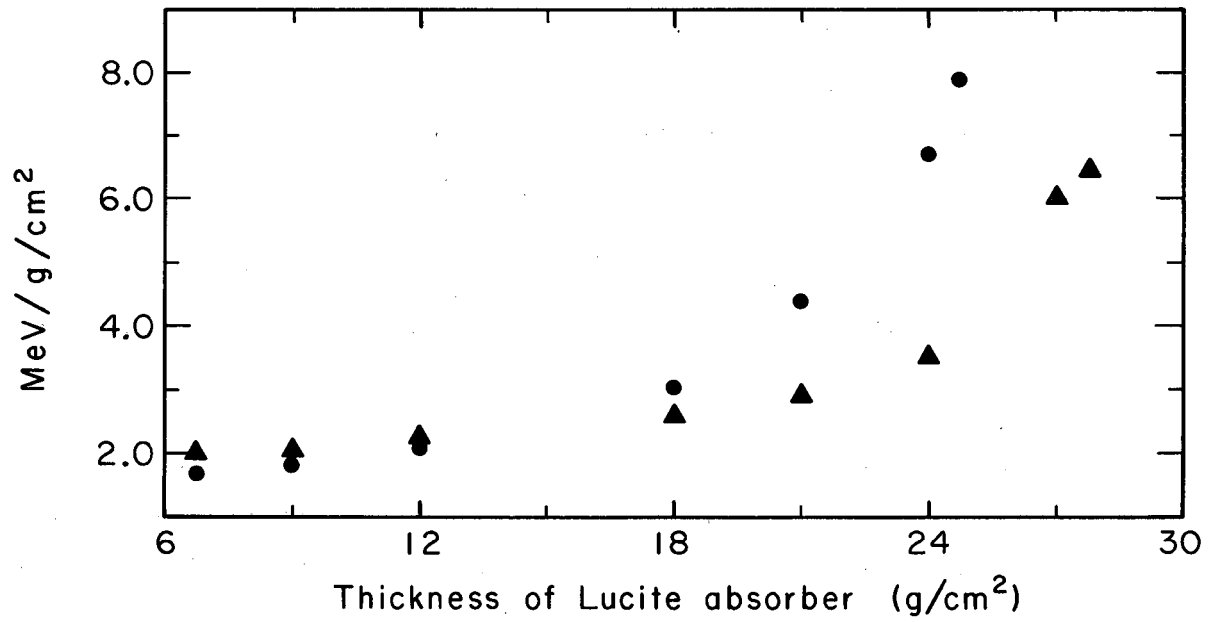
Fig. 30. Horizontal beam profile for 101-MeV π^- meson beam.

- no absorber
- 4-inch Lucite absorber
- ▲ 7.5-inch Lucite absorber

ionization potential. In this case, the effective chamber thickness corresponds to almost 90% of the total proton range, and is 22 times as great as the range of a 6-MeV α particle. That is, we are still absorbing only a small fraction of the proton energy from the stars, but we should now see almost all the energy from alpha fragments regardless of where the star event occurs in the chamber. The nitrogen filling used in the chamber was of high purity. This is an important consideration for high gas pressures, since it has been shown that the presence of even small impurities of such molecules as O_2 or H_2O (where the electron-attachment coefficient is very high) can cause a considerable fraction of the electrons to form negative ions and thereby increase ionization losses through recombination.⁶⁵

Before the measurements with the high-pressure chamber were made, a Bragg curve was obtained with a low-pressure chamber (2 psi above atmospheric) filled with nitrogen. The purpose of these measurements was twofold: (a) since the integral range curve has furnished us number-distance information, we can now make an estimate of the probable energy loss per pion from the experimental data and check its agreement with theoretical calculation; (b) the results should be useful for comparison purposes with the high-pressure chamber measurements.

The total energy deposited by pions only, in a distance equal to the chamber thickness, was first calculated from the chamber results and expressed in $MeV/g/cm^2$. This quantity was then converted to $MeV/g/cm^2$ per pion, taking the number of pions at each depth from the integral range data. The approximate results are compared with theoretical calculation for the probable energy loss of a single particle in Fig. 31. The agreement is very good in the initial part of the curve. This is because the straggling that results from the statistical fluctuations in energy loss has not yet become important. However, as we approach the Bragg peak the relative homogeneity of the beam is lost and the calculation for the probable energy loss of a single particle can no longer be applied to a beam of particles. Owing to the statistical



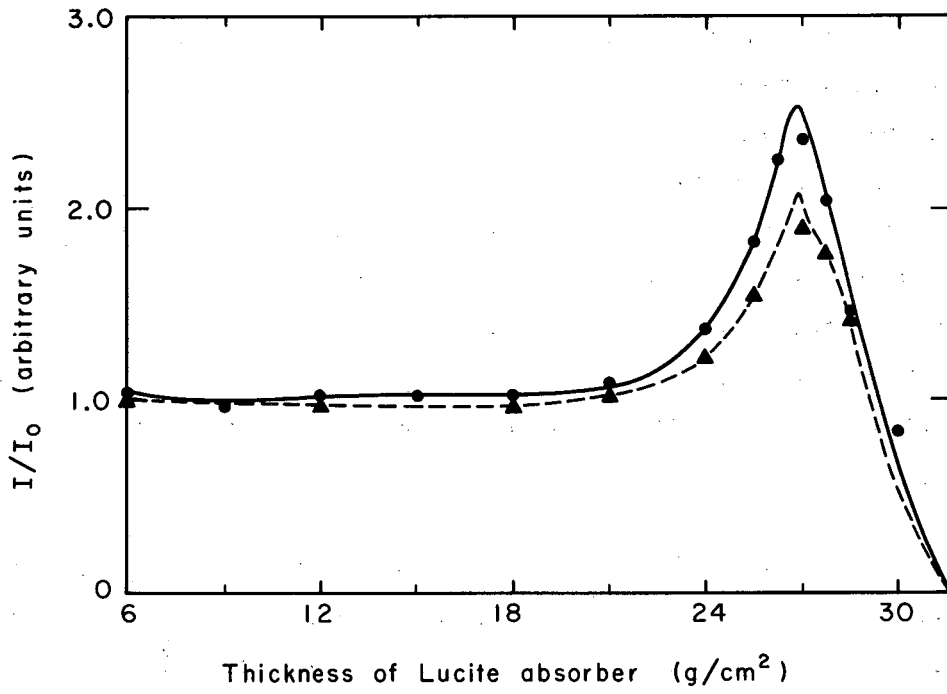
MU-34199

Fig. 31. Most probable energy loss for 101-MeV pions.
● calculated
▲ experimental

fluctuation in the amount of energy lost by a particle, and its associated fluctuations in range, there is no longer a single definable residual energy remaining at a certain depth in the absorber, but a spectrum of energies. This departure from the theoretical single-particle pattern of energy loss and the change in the energy spectrum that accompanies it are reflected in the experimentally determined values for the energy loss. For example, at a depth of 7 inches of Lucite (which corresponds to the base of the Bragg peak), the measured value for the probable energy loss per pion is 3.5 MeV/g/cm^2 , compared with the single-particle value of 4.4 MeV/g/cm^2 . As we go deeper into the Lucite the difference between the quantities increases. It should be mentioned again that these experimentally determined values for energy loss represents an average over the effective volume of the chamber, and are probably lower than one would get with a smaller chamber. A comparison of low- and high-pressure chamber Bragg curves is shown in Fig. 32.

The low-pressure curve agrees well with results from the earlier, argon-filled ion chamber. Because of the increased intensity that was noted earlier, the dose at the Bragg peak has been increased from a value of 3.5 mrad/min for runs #1 and #2 to a value for this run of about 140 mrad/min. The peak-to-plateau ratio has decreased from almost 3 for the argon data to 2.53 for the nitrogen results, while the FWHM has increased from about 1 inch to almost 2 inches. This change can be readily explained by two factors: (a) there has been an increase in the momentum spread of the pion beam from 5% in runs #1 and #2 to almost 9% in this run, (b) the energy of the incident pion beam used in runs #1 and #2 was 90 MeV, while in run #3 the energy was 101 MeV. The increased range for the higher-energy pions leads to an increased straggling, which in turn depresses the peak.

On the other hand, the comparison of the results for low- and high-pressure chambers is contrary to what one would expect. Although the peak is positioned at the same depth in Lucite for both chambers, the height of the peak for the high-pressure chamber was 17% less than

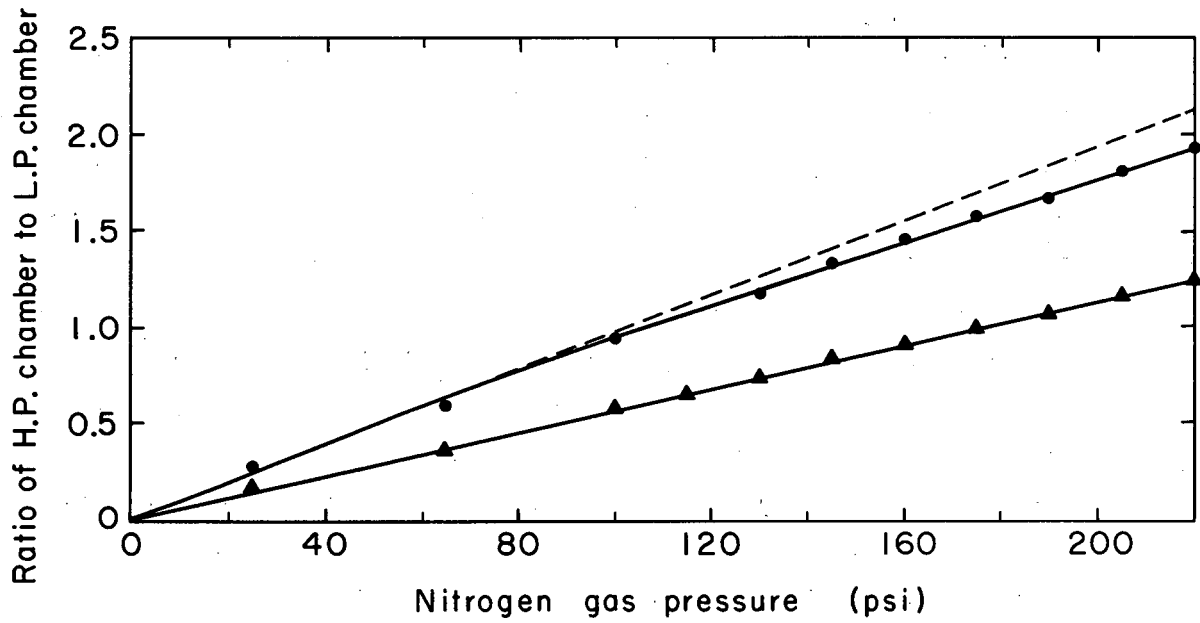


MU-34200

Fig. 32. Bragg curve for 101-MeV π^- mesons in nitrogen-filled ion chamber.
● low pressure
▲ high pressure

that for the low-pressure chamber. It was thought at first that this unexpected result might be partly due to recombination losses associated with relatively intense ionization caused by star fragments at the peak. In order to test for possible ion-collection losses, a recheck of the high-voltage plateau for the high-pressure chamber was performed with the chamber positioned at the Bragg peak. The results show that the collection losses were negligible.

A second consideration was to examine the response of the chamber as a function of gas pressure. Since the energy loss of a charged particle is directly proportional to the electron density of the medium traversed, an increase in gas pressure (with its associated increase in density) should cause an equivalent increase in chamber response. The response of the chamber to this test is shown in Fig. 33. The chamber was alternately placed at two positions on the Bragg curve and a pressure-vs-response curve was obtained for each position, with the low-pressure chamber serving as monitor. The measurements made at a Lucite depth of 6 g/cm^2 exhibit a linear relationship which extrapolates to zero response for zero gas pressure. On the other hand, the values obtained at 27 g/cm^2 of Lucite are not strictly linear, so they do not extrapolate to zero. If we assume zero response at zero gas pressure and extend a line from this point to higher gas pressures, we obtain the dotted line shown in Fig. 33. A comparison of this line with the experimentally determined values reveals a reduction in the chamber response above 80 psi which becomes greater with increasing pressure. At approximately 220 psi this departure of the measured values from the hypothetical dotted line represents a 12% decrease in response of the chamber. That is, for a gas-filling pressure of approximately 220 psi, the chamber reading is 12% too low. Perhaps this behavior partly explains the relative responses of the low- and high-pressure chambers shown in Fig. 33. Despite this explanation, it is still difficult to understand why observed high-pressure chamber response was not greater. Much work remains to be done to more fully explain this behavior.



MU-34201

Fig. 33. Response of high-pressure chamber to changes in pressure of gas filling.

- high-pressure chamber at 27 g/cm² depth in Lucite (at Bragg peak)
- ▲ high-pressure chamber at 6 g/cm² depth in Lucite

V. CONCLUDING REMARKS

In summary, it seems reasonable to say that the results discussed in this thesis are generally very encouraging. I believe that the evidence reported here is indicative of many possible advantages in the use of π^- mesons for radiotherapy.

The tumor-skin ratio of 2.96 with a 1-inch-wide Bragg peak (measured at half maximum for a 91-MeV π^- -meson beam with $\approx 5\%$ momentum spread) suggests that these particles should be particularly useful in giving uniform irradiation of large volumes encompassed by the Bragg peak. Measurements were also made for a 101-MeV π^- -meson beam with 8.6% momentum spread, indicating a tumor-skin dose rate of 2.53 and a Bragg peak width, measured at half maximum, of almost 2 inches. On the basis of these results, it would appear that one may, by proper choice of the momentum spread of the pion beam, select a Bragg peak width appropriate to the size of the tumor being irradiated.

The energy of the incident pion beam is also important, since the effect on the tumor-skin ratio of the lateral dispersion of the beam due to Coulomb scattering is to reduce this ratio with increasing pion energy (or range). Since the maximum depth at which it is commonly necessary to irradiate tumors in the human body is about 10 cm (which corresponds to the range of a 52-MeV pion), we should expect to improve the tumor-skin ratio by employing pions of roughly half the energy used in this experiment. In any case, the tumor-skin ratio mentioned above, in all probability, represents the minimum value one would expect for pions of that energy, since the ion chambers used were found to be sensitive to electronic events only. Indeed, the solid-state detector, which is relatively insensitive to electronic events but optimized to detect the α star fragments, has indicated a tumor-skin dose ratio of 17, which is greater than the ion chamber results by almost a factor of six. Although the reliability of this value certainly should be

experimentally investigated further, it has been shown to be by no means an unreasonable result.

The highest dose actually measured in this experiment was 140 mrad/min. However, this measurement was made at the Bragg peak with an ion chamber, and therefore includes very little energy from the nuclear fragments. A correction for this effect, based on the solid-state results, yields a dose value which is 5.75 times as great as the ion chamber value, or 805 mrad/min. Moreover, these dose values are for a beam intensity of $\approx 2 \times 10^4 \pi^- / \text{cm}^2 \text{ sec}$. This intensity could probably be increased by a factor of at least ten or twenty by employing a second stage of focusing, which would allow a large fraction of the beam to be focused into a spot a few cm^2 in area. Perhaps the intensity may be improved even further by choosing a target element with a higher Z than beryllium.

The effect of the Bragg peak should be enhanced by an increased RBE (relative biological effectiveness) resulting from the higher LET (linear energy transfer) in this region. Since there is at present no precise information relating either of these values for pions, the next few experiments have been designed to specifically investigate these areas. The lithium-drifted solid-state detector with its larger depletion layer promises to be particularly effective in securing a more definitive appraisal of the nuclear fragment energy available and in evaluating the LET associated with these fragments. Preliminary studies have already been begun with this detector, using protons and α particles of various energies, and will be extended to π^- mesons very soon.

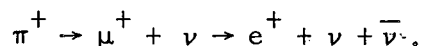
The other part of this problem--namely, an appraisal of the RBE resulting from the LET that is observed--is to be performed by studies relating the differential effect of the Bragg peak to the initial portion of the Bragg curve for different biological systems. Preparations are presently being made to perform such a study with Vicia faba and ascites tumor cells.

The lateral spread of the beam, which is due to Coulomb scattering and was measured perpendicular to the initial beam toward the end of the pion range, was approximately 1.25 inches. Use of a 52-MeV pion beam would reduce the lateral spreading of the beam by about a factor of two.

A study of the loss of pions from the 101-MeV pion beam owing to inelastic nuclear scattering indicated that about 60% of the original pions persisted to the end of the range and were available for nuclear capture and the subsequent star event. That is, approximately 40% of the pions were lost from the beam before the Bragg peak was reached. This loss also should be reduced considerably by the use of a lower-energy pion beam.

Still another factor to consider is the beam contamination. Muon and electron contaminations of the order of 12% and 24%, respectively, were measured in this experiment. Although the degree of electron contamination of a pion beam increases with decreasing pion energy, the fractions of electrons can be minimized by proper control of the magnet system, or eliminated completely by electrostatic separation.

Although this study was mainly concerned with the behavior of the π^- meson, and π^+ mesons were of interest only insofar as they served this end, it became apparent during the course of the experiment that π^+ mesons had some important advantages of their own. From photographic film we received evidence of a very intense region of ionization at the end of the π^+ range, which we have attributed to positrons of 35 MeV average energy resulting from the decay of the π^+ meson according to



Except for the nuclear capture process at the end of the π^- -meson range, with its subsequent star event, π^+ and π^- mesons of the same initial energy behave alike in their traversal of matter and therefore they exhibit identical ranges. The behavior of the π^+ meson at the end

of its range could be very important in attacking the problem of precisely locating the position of the Bragg peak deep in the body despite the heterogeneity of the absorbing medium. A counter telescope arrangement could be used to detect the emitted positrons and to determine their points of origin, thereby locating the end of the range for π^+ mesons (which is also the range of π^- mesons). In principle, then, the π^+ beam could serve to locate the region of treatment deep in the body while the π^- beam could be used for the actual treatment of that region. However, this application of pions to therapy is still in its conceptual stage, and must await confirmation by experimental investigation.

ACKNOWLEDGMENTS

I would like to express my gratitude to Professor Chaim Richman for his guidance and encouragement throughout this study. I am also indebted to Professor Frederick J. Bante and Professor Frank Harrison for their continuing interest in this research.

Special mention is also due Dr. M. R. Raju for his generous assistance and helpful advice throughout this experiment. Thanks are due to Mr. Nick Yanni for his efficient technical support and to the many members of the Bio-Medical group, who cooperated so fully with us. Also, I wish to thank Mr. James Vale and the cyclotron crew for their assistance and cooperation during the running of the experiment.

Professor John H. Lawrence and Professor Cornelius Tobias are to be gratefully acknowledged for making the facilities at Berkeley (under the auspices of the U. S. Atomic Energy Commission) available for this study. The financial support of this program by the American Cancer Society is also appreciated.

Finally, I am especially indebted to the Gilbert X-Ray Company for their financial assistance which made my graduate studies possible.

BIBLIOGRAPHY

1. John S. Laughlin, *Physical Aspects of Betatron Therapy* (Charles C. Thomas, Springfield, Ill., 1954).
2. K. A. Wright, R. C. Granke, and J. G. Trump, *Physical Aspects of Megavolt Electron Therapy*, *Radiology* 67, 553 (1956).
3. L. V. Spencer and V. Fano, *Energy Spectrum Resulting from Electron Slowing Down*, *Phys. Rev.* 43, 1172 (1954).
4. Symposium on Radiobiology, Edited by J. J. Nickson (John Wiley and Sons, Inc. New York, 1952), p. 28.
5. C. A. Tobias, H. O. Anger, and J. H. Lawrence, *J. Roentgenol.* 67, 1 (1952).
6. B. Larsson, T. Suedberg, and H. Tyren, 1952-56 Yearbook for the Swedish Cancer Society (Stockholm, 1956), p. 41.
7. S. D. Warshaw and D. G. Oldfield, *Am. J. Roentgenol.* 78, 876 (1957).
8. J. H. Lawrence, P. C. Aegersold, and E. O. Lawrence, *The Comparative Effects of Neutrons and X-Rays on Normal and Neoplastic Tissue*, *Am. Assoc. Adv. Sci. No. 4*, 215 (1937).
9. R. S. Stone, J. H. Lawrence, and P. C. Aegersold, *Preliminary Report on Use of Fast Neutrons in Treatment of Malignant Disease*, *Radiology* 35, 322 (1940).
10. J. F. Fowler, R. L. Morgan, C. A. P. Wood, D. K. Bewley, R. H. Thomlinson, S. Hornsey, G. Silini, and T. Alper, *Pre-Therapeutic Experiments with the Fast Neutron Beam from the Medical Research Council Cyclotron*, *Brit. J. Radiol.* 36, 77 (1963).
11. J. H. Lawrence, C. A. Tobias, J. L. Born, C. L. Wang, and J. H. Linfoot, *Heavy-Particle Irradiation in Neoplastic and Neurologic Disease*, *J. Neurosurg.* 19, 717 (1962).

12. R. N. Kjellberg and others, Biological and Clinical Studies using the Bragg Peak of the Proton Beam, paper presented at the Second International Congress of Radiation Research, Harrogate, England, August 1962.
13. R. E. Zirkle, The Radiobiological Effectiveness of Alpha Particles as a Function of Ion Concentration Produced in their Paths, *Am. J. Cancer* 23, 558 (1935).
14. G. W. Berendsen, *Nature* 193, 1153 (1962).
15. G. W. Berendsen, T. Beusker, A. Vergroesen, and L. Bydka, *Radiation Res.* 13, 841 (1960).
16. J. H. Lawrence, K. Sillesen, and J. T. Lyman, Heavy-Particle Ionization and the Proliferative Capacity of Neoplastic Cells In Vivo, in *Biology and Medicine Semiannual Report, Lawrence Radiation Laboratory Report UCRL-11033*, Spring 1963.
17. B. Larsson and B. A. Kihlman, Chromosome Aberrations following Irradiations with High Energy Protons and their Secondary Radiations, *Intern. J. Radiation Biol.* 2, 8 (1960).
18. B. Larsson, Pretherapeutic Physical Experiments with High Energy Protons, *Brit. J. Radiol.* 34, 143 (1961).
19. C. A. Tobias, D. C. Van Dyke, M. E. Simpson, H. O. Anger, R. L. Huff, and A. A. Koneff, *Am. J. Roentgenol., Radium Therapy, Nucl. Med.* 72, 1 (1954).
20. G. Schwarz, *Muench. Med. Wochenschr.* 56, 1217 (1909).
21. P. Alexander, *Radiation Res.* 6, 653 (1957).
22. I. Churchill-Davidson, Oxygen Effects on Radiosensitivity, in Proceedings of the Conference on Research on the Radiotherapy of Cancer, 1961 (American Cancer Society, Inc., 1961).
23. P. Howard-Flanders and T. Alper, The Sensitivity of Microorganisms to Irradiation Under Controlled Gas Conditions, *Radiation Res.* 1, 518 (1957).
24. G. W. Berendsen, in Symposium on The Initial Effects of Ionizing Radiation on Cells, Moscow, 1961 (Academic Press, New York, 1961).

25. L. H. Gray, A. D. Conger, M. Ebert, S. Hornsey, and O. Scott, Brit. J. Radiol. 26, 638 (1953).
26. S. Hornsey and G. Silini, Comparison of X-Rays and Cyclotron Neutrons on Mouse Ascites Tumor, Mouse Testis, and Chick Embryos, Brit. J. Radiol. 36 92 (1963).
27. H. B. Hewitt and C. W. Wilson, Brit. J. Cancer 13, (1959).
28. C. A. Tobias, High-Energy Radiations in Biological Research and Therapeutic Investigation, in the Joint Committee of Atomic Energy Hearings of March 27, 1961.
29. P. H. Fowler and D. H. Perkins, The Possibility of Therapeutic Applications of Beams of Negative Pi Mesons, Nature 189, 525 (1961).
30. A. Astbury, K. M. Crowe, J. G. Deutsch, Tin Maung, and R. E. Taylor, Study of Optimum Target Positions for the Secondary Meson Beams from the 184-inch Cyclotron, Lawrence Radiation Laboratory Report UCRL-10120, March 1962 (unpublished).
31. O. Chamberlain, Optics of High-Energy Beams, Ann. Rev. Nucl. Sci. 10, 161 (1960).
32. J. Good, M. Pripstein, and H. Goldberg, Cyclotron Orbits: A 709 Ray-Trace Program for Cylindrically Symmetric Magnetic Fields, Lawrence Radiation Laboratory Report UCRL-11044, October 1963 (unpublished).
33. T. J. Devlin, OPTIK: An IBM 709 Computer Program for the Optics of High-Energy Particle Beams, Lawrence Radiation Laboratory Report UCRL-9727, September 1961 (unpublished).
34. J. Solomon and S. Andrae, Rev. Sci. Instr. 34, 1126 (1963).
35. A. C. Birge, C. A. Tobias, and H. O. Anger, Heavy Charged Particle Beams, in Radiation Dosimetry, G. H. Hine and G. L. Brownell, Eds. (Academic Press, Inc., New York, 1956), p. 624.

36. M. Rich and R. Madey, Range-Energy Tables, University of California Radiation Laboratory Report UCRL-2301, March 1954 (unpublished).
37. Walton A. Perkins III, Positive Pion Production by Negative Pions (thesis), Lawrence Radiation Laboratory Report UCRL-8778, June 1959 (unpublished).
38. V. Perez-Mendez and J. Atkinson, Gas Cerenkov Counters, *Rev. Sci. Instr.* 30, 19 (1959).
39. J. W. Boag, Ionization Chambers, in Radiation Dosimetry, G. H. Hine and G. L. Brownell, Eds. (Academic Press, Inc., New York, 1956), p. 153.
40. F. Goulding, A Survey of the Applications and Limitations of Various Types of Detectors in Radiation Energy Measurements, Lawrence Radiation Laboratory Report UCRL-11302, February 1964 (unpublished).
41. C. Williamson and J. P. Boujot, Tables of Range and Rate of Energy Loss of Charged Particles of Energy 0.5 to 150 MeV, Saclay Report CEA 2189, 1962.
42. E. Tochilin, B. W. Shumway, G. D. Kohler, Response of Photographic Emulsion to Charged Particles and Neutrons, *Radiation Res.* 4, 467 (1956).
43. N. Bohr, *Phil. Mag.* 24, 10 (1913); 30, 581 (1915).
44. V. Fano, Penetration of Protons, Alpha Particles, and Mesons, *Ann. Rev. Nucl. Sci.* 13, 1 (1963).
45. F. Bloch, *Z. Physik* 81, 363 (1933).
46. W. F. G. Swann, *J. Franklin Inst.* 226, 598 (1938).
47. H. Bethe and J. Ashkin, The Passage of Heavy Particles Through Matter, in Experimental Nuclear Physics, Volume I, E. Segrè, Ed. (John Wiley and Sons, Inc., New York, 1963), p. 166.

48. T. J. Thompson, Effects of Chemical Structure on Stopping Powers for High-Energy Protons (thesis), University of California Radiation Laboratory Report UCRL-1910, August 1952 (unpublished).
49. L. Landau, On the Energy Loss of Fast Charged Particles by Ionization, *J. Phys.* 8, 201 (1944).
50. W. McMillan and E. Teller, *Phys. Rev.* 72, 1 (1947).
51. Robert E. Marshak, Meson Physics (McGraw-Hill, New York, 1952).
52. W. H. Barkas, *Phys. Rev.* 75, 1109 (1949).
53. S. Jones and R. White, *Phys. Rev.* 78, 12 (1950).
54. Bruno Rossi, High Energy Particles (Prentice-Hall, Inc., Englewood Cliffs, New Jersey, 1952).
55. G. Bernardini, E. Booth, and L. Lederman, *Phys. Rev.* 83, 1075 (1951);
G. Bernardini, E. Booth, L. Lederman, and J. Tinlot, *Phys. Rev.* 82, 105 (1951).
56. R. Leighton, C. Anderson, and A. Seriff, *Phys. Rev.* 75, 1942 (1949).
57. E. Gardner, W. Barkas, F. Smith, H. Bradner, *Science* 111, 191 (1950).
58. M. G. K. Menon, H. Muirhead, and O. Rochat, *Phil. Mag.* 41, 583 (1950).
59. W. Cheston and L. J. B. Goldfarb, *Phys. Rev.* 78, 683 (1950).
60. P. Ammiraju and L. Lederman, *Nuovo Cimento* 4, 283 (1956).
61. W. Aron, B. G. Hoffman, and F. C. Williams, Range-Energy Curves, University of California Radiation Laboratory Report UCRL-121, July 1960 (unpublished).
62. S. Falkmer, B. Fors, B. Larsson, A. Lindell, J. Naeslund, and S. Stenson, Pilot Study on Proton Irradiation of Human Carcinoma, *Acta Radiol.* 58, 33 (1962).

63. Eugene Tochilin (United States Naval Radiological Defense Laboratory), private communication, 1963.
64. Tin Maung (Lawrence Radiation Laboratory, private communication).
65. B. Wilson, L. Beghian, C. Collic, H. Halban, and G. Bishop, Rev. Sci. Instr. 21, 699 (1950).

VITA

Henry Aceto, Jr., was born in Schenectady, New York, on July 12, 1935, the son of Gilda Finnegan and the late Henry Aceto, Sr. After completing his work at Scotia High School, Scotia, New York, in 1954, he entered the State University of New York, at Albany. In 1955, he married Karlene Ferbee Johnson of Schenectady, New York. A son, Steven Thomas, was born in 1956, and a daughter, Nanci Marie, was born in 1960. He received the degree of Bachelor of Science from the State University of New York in June, 1958. During the following year and one-half he was employed as health physicist at the Knolls Atomic Power Laboratory, Schenectady, New York. In March, 1959, he was granted an Atomic Energy Commission Special Fellowship in Radiological Physics, and in September, 1959, he entered the Graduate School of the University of California, Berkeley. He was awarded the degree of Master of Science in June 1961. From June 1960 to August 1962 he was employed as physicist in the Health Physics Department at the Lawrence Radiation Laboratory (University of California), Berkeley. In the fall semester of 1961 he taught an evening course in Radiation Safety at Oakland City College. In September 1962 he was granted the Gilbert X-ray Company Predoctoral Fellowship in Radiation Physics and Radiobiology, and since that time he has been enrolled in the Graduate School of The University of Texas. His writings include: Calibration Techniques for Radiation Survey Instrumentation, Knolls Atomic Power Laboratory Report KAPL-HP1; and Lawrence Radiation Laboratory Reports (1) Neutron Depth Dose from (α , n) and (γ , n) Sources in a Tissue-Equivalent Phantom, UCRL-40267, March 1963; (2) Variation of the Fission Flux Fast Reactor Measured Over Large Distances, UCRL-10364, Oct. 1962, and (3) Neutron Tissue Dose at Large Distances from an Elevated Unshielded Reactor, UCRL-10559, March 1963.

Permanent address: 1851 Yosemite Road, Berkeley 7, California

This dissertation was typed by: Carmen Claire Aspuria and June Mosher

This report was prepared as an account of Government sponsored work. Neither the United States, nor the Commission, nor any person acting on behalf of the Commission:

- A. Makes any warranty or representation, expressed or implied, with respect to the accuracy, completeness, or usefulness of the information contained in this report, or that the use of any information, apparatus, method, or process disclosed in this report may not infringe privately owned rights; or
- B. Assumes any liabilities with respect to the use of, or for damages resulting from the use of any information, apparatus, method, or process disclosed in this report.

As used in the above, "person acting on behalf of the Commission" includes any employee or contractor of the Commission, or employee of such contractor, to the extent that such employee or contractor of the Commission, or employee of such contractor prepares, disseminates, or provides access to, any information pursuant to his employment or contract with the Commission, or his employment with such contractor.

Faint, illegible text covering the majority of the page, possibly bleed-through from the reverse side.

